Chapter 3

Nonlinear Dynamics and Its Applications in Nanocantilevers

Najib Kacem

FEMTO-ST Institute—UMR 6174, Department of Applied Mechanics, University of Franche-Comté, 24 chemin de l'Épitaphe, 25000 Besançon, France

najib.kacem@femto-st.fr

3.1 Introduction

Nanoelectromechanical systems (NEMS) are drawing interest from the scientific community for a wide range of applications due to their unique properties. Nanocantilevers are among those of the possible NEMS realizations that offer access to fundamental resonant frequencies in the microwaves and active masses in the femtograms. Nanocantilever have been proposed for ultrafast sensors and actuators, signal processing components, quantum computing (Bose and Agarwal, 2006), and ultra sensitive force (Jiang et al., 2008) and mass (Li et al., 2007) detection.

Actually, it is a challenge to optimize NEMS mass sensors in order to achieve high resolutions. Although the linear design optimization and mechanical transduction gain of the devices have been thoroughly studied, the drive power has always been a priori limited by the onset of nonlinearities. Indeed, driving the

Nanocantilever Beams: Modeling, Fabrication, and Applications
Edited by Ioana Voiculescu and Mona Zaghloul

ISBN 978-981-4613-23-1 (Hardcover), 978-981-4613-24-8 (eBook)
www.panstanford.com

cantilever at large oscillation amplitude leads to better signal to noise ratio (SNR) and, thus, simplifies the design of the electronic feedback loop. However, doing so in the nonlinear regime reduces the sensor performances since the frequency instability of a nonlinear resonator is proportional to its oscillation amplitude. Moreover, even when NEMS resonators are used as oscillators in closed-loop, a large part of noise mixing (Kaajakari et al., 2005b) due to nonlinearities drastically reduces their dynamic range and alters their detection limit. NEMS cantilevers are promising candidates for the new generation of physical, chemical and biological sensing. One reason for this is that they are commonly said to have a very large linear dynamic range compared to clamped-clamped nanoresonators, without any formal proof, quantitative comparison, or thorough study. Models for doubly clamped beams (Kacem et al., 2009, 2011b) cannot be easily adapted to cantilevers: indeed, their real specificity comes from their complex nonlinear dynamics including geometric and inertial nonlinearities. This partly explains why so little has been done about nonlinear dynamics of electrostatically actuated cantilevers.

The nonlinear dynamics of cantilevers have received considerable attention because of their importance in many engineering applications. Crespo da Silva and Glynn (1978a,c) derived a set of integro-partial-differential equations governing flexural-flexural-torsional motions of inextensional beams, including geometric and inertia nonlinearities. They used these equations and the method of multiple scales to ascertain the importance of the geometric terms for the lower modes, especially the first mode. These equations have been also used for several investigations such as the non-planar responses of cantilevers to principal parametric and primary resonant excitations (Nayfeh and Pai, 1989; Pai and Nayfeh, 1990), the nonlinear response of an inextensional beam to a primary resonant excitation of one of its flexural modes when the first torsional frequency is of the same order as the lower flexural frequencies (da Silva and Zaretzky, 1994; Zaretzky and da Silva, 1994), as well as the nonlinear non-planar response of cantilever inextensional metallic beams to a parametric excitation of order two its flexural modes (Arafat et al., 1998). Chowdhury et al. (2005) provided a close-form model for the static pull-in voltage of electrostatically actuated cantilevers without including

the geometric nonlinearities. Ahmadian et al. (2009) employed a finite element formulation for the dynamic analysis of nonlinear Euler cantilevers electrostatically actuated including main sources of nonlinearities, but the resonant case has not been considered. Liu et al. (2004) simulated an electrostatically controlled cantilever microbeam and qualitatively showed period-doubling bifurcation, chaos, Hopf bifurcation, and strange attractors using the Poincaré map method, which are hardly exploitable by MEMS and NEMS designers.

In this chapter, the physical limitations in NEMS mass sensors when operating beyond their critical amplitudes are investigated. Based on the nonlinear dynamics of nanomechanical cantilevers, the main idea is to provide simple analytical tools for NEMS designers in order to optimize mass resonant sensors designs and enhance their performances for precision measurement applications such as mass spectrometry.

3.2 Resonant Sensor Specifications

3.2.1 Mechanical Analysis

The mechanics of a resonant cantilever is theoretically investigated as an important step towards the determination of the resonance frequency and the sensitivity expressions. Then, based on the resonator dynamic response, the transfer function is deduced which will be used in an advanced step for noise analysis.

3.2.1.1 Resonance frequency

Assuming that the nonlinear terms are negligible, the equation of motion of a beam in bending subjected to an axial tensile force (F) can be written as

$$EI\frac{\partial^4 \tilde{w}}{\partial \tilde{x}^4} + \xi\frac{\partial \tilde{w}}{\partial \tilde{t}} - F\frac{\partial^2 \tilde{w}}{\partial \tilde{x}^2} + \rho A\frac{\partial^2 \tilde{w}}{\partial \tilde{t}^2} = 0, \tag{3.1}$$

where E is Young's modulus, I is the bending moment of inertia, ξ is the viscous damping coefficient, ρ is the material density and A is the beam section. The solution $\tilde{w}(\tilde{x},\tilde{t})$ can be solved by the method of separation of variables where

$$\tilde{w}(\tilde{x},\tilde{t}) = \phi(\tilde{x}) \cdot a(\tilde{t}) \tag{3.2}$$

The equation of the beam mode shapes with respect to the position coordinate $\tilde{x}$ can be written as

$$\phi(\tilde{x}) = C_1 \cos\left(\frac{\lambda\tilde{x}}{L}\right) + C_2 \sin\left(\frac{\lambda\tilde{x}}{L}\right) + C_3 \cosh\left(\frac{\lambda\tilde{x}}{L}\right) + C_4 \sinh\left(\frac{\lambda\tilde{x}}{L}\right) \tag{3.3}$$

Constants C_1–C_4 can be evaluated depending on the boundary conditions of the resonator; λ is a dimensionless parameter related to the wavelength, and it depends on the mode shape and the resonator boundary conditions. It can be evaluated numerically as listed in Table 3.1 for several bending modes of cantilevers as well as clamped-clamped beam resonators.

Table 3.1 Dimensionless parameter λ for the first four eigenfrequencies of cantilevers and c-c beams.

Mode/λ	Cantilever beam	Clamped-clamped beam
Mode 1	1.875	4.730
Mode 2	4.694	7.854
Mode 3	7.855	11.00
Mode 4	10.995	14.14

Using the Galerkin method, the time dependence can be cast in the form of a mass-spring-damper equation:

$$M_{\text{eff}}\ddot{a} + B_{\text{eff}}\dot{a} + K_{\text{eff}}a = 0, \tag{3.4}$$

where expressions for M_{eff} and K_{eff} can be written as (Roessig, 1998)

$$FM_{\text{eff}} = \int_0^L \rho A \phi^2(\tilde{x}) d\tilde{x} \tag{3.5}$$

$$K_{\text{eff}} = \frac{EI}{L^3}\int_0^L \left(\frac{\partial^2\phi}{\partial\tilde{x}^2}\right)^2 d\tilde{x} + \frac{F}{L}\int_0^L \left(\frac{\partial\phi}{\partial\tilde{x}}\right)^2 d\tilde{x} \tag{3.6}$$

Thus, for a null axial force, the resonator natural frequency is

$$f_0 = \frac{1}{2\pi}\sqrt{\frac{K_{\text{eff}}(F=0)}{M_{\text{eff}}}} \tag{3.7}$$

3.2.1.2 Sensitivity

For a resonator vibrating in its fundamental mode, the natural frequency for a constant axial force (F) along the length of the beam can be written in terms of the nominal resonant frequency by evaluating the integrals in Eqs. (3.5) and (3.6).

$$f = f_0\sqrt{1 + F \cdot S} \tag{3.8}$$

$$S = \frac{\rho A L^2 \int_0^L \phi^2(\tilde{x})d\tilde{x} \int_0^L \left(\frac{\partial \phi}{\partial \tilde{x}}\right)^2 d\tilde{x}}{EI\int_0^L \left(\frac{\partial^2 \phi}{\partial \tilde{x}^2}\right)^2 d\tilde{x}} \tag{3.9}$$

Thus, the force sensitivity of the resonator (mechanical scale factor) can be written as

$$SF_{\text{f}} = \frac{S}{2} f_0 \tag{3.10}$$

In the same way, the mass sensitivity of the resonator can be deduced as

$$SF_{\text{m}} = \frac{1}{2M_{\text{eff}}} f_0 \tag{3.11}$$

3.2.1.3 Dynamic response

The starting point for the simplest dynamic analysis is the characteristic differential equation describing the evolution of the displacement of the resonating element subjected to a linear time-varying drive force F_{d}.

$$M_{\text{eff}}\ddot{a} + B_{\text{eff}}\dot{a} + K_{\text{eff}}a = F_{\text{d}}\cos(\Omega\tilde{t}), \tag{3.12}$$

where Ω is the drive frequency. Equation (3.12) can be written in its canonical form as

$$\ddot{a} + \frac{\omega_0}{Q}\dot{a} + \omega_0^2 a = \frac{F_{\text{d}}}{M_{\text{eff}}}\cos(\Omega\tilde{t}), \tag{3.13}$$

where $\omega_0 = 2\pi f_0$ and Q is the resonator quality factor that can be estimated by evaluating the different system losses. Using the Fourier transform, the resonator transfer function can be deduced as follows

$$H(\Omega) = \frac{\frac{1}{M_{\text{eff}}}}{\Omega^2 - \omega_0^2 + j\frac{\Omega\omega_0}{Q}} \tag{3.14}$$

For MEMS and NEMS designers, the quality factor is an important parameter, since it defines the sensor bandwidth. Moreover, as shown in Eq. (3.14), the resonator transfer function depends on Q. Hence, it is important to estimate correctly the quality factor.

3.2.2 Quality Factor

The mechanical quality factor Q is a measure for the energy losses of a resonator or in other words, a measure for the mechanical damping. The Q-factor is defined as the ratio between the total energy stored in the vibration and the energy loss per cycle:

$$Q \approx 2\pi \frac{\text{total energy stored in vibration}}{\text{dissipated energy per period}} \tag{3.15}$$

Low energy losses imply a high Q-factor. The Q-factor cannot be determined directly, but instead can be deduced from the response characteristics of the resonator. One common method of determining Q is from the steady-state frequency plot of a resonator excited by a harmonic force with constant amplitude:

$$Q \approx \frac{\omega_{\text{res}}}{\Delta\omega_{-3\,\text{dB}}}, \tag{3.16}$$

where ω_{res} is the frequency with maximum frequency response and $\Delta\omega_{-3\,\text{dB}}$ is the half-power bandwidth of the frequency response.

In nanomechanical resonators, there are numerous possible sources of dissipation, which may broadly be classified as either intrinsic or extrinsic. Intrinsic sources of dissipation, such as phonon–phonon and phonon–electron interactions, result from properties of the resonating material, whereas extrinsic sources, such as gas friction, clamping loss, and surface loss, result from

interactions with the environment. Obviously, little can be done to control dissipation from intrinsic sources other than careful choice of resonator material. Theoretical calculations have shown that these intrinsic sources of dissipation are small compared to the dissipation currently exhibited by nanomechanical resonators.

There are many extrinsic mechanisms of dissipation in nanomechanical resonators. They can be listed by their origin as follows:

3.2.2.1 Gas friction

At pressures above approximately 1 torr, viscous damping of a resonator by the surrounding gas is the dominant form of dissipation (Ekinci and Roukes, 2005). Here, the energy is radiated as sound. Fortunately, it is easy to achieve lower pressures where viscous damping no longer dominates. At these lower pressures, where the mean free path of the gas molecules is much larger than the relevant sound wavelength, energy may still be dissipated through momentum transfer to individual molecules. In this case, the dissipation is expressed as

$$Q_{\text{gas}}^{-1} = \frac{pA}{M_{\text{eff}}\omega_{\text{r}}v}, \tag{3.17}$$

where p is the pressure, A is the surface area, M_{eff} is the effective mass of the resonator, ω_{r} is the resonator angular frequency, and v is the thermal velocity of the gas. According to Eq. (3.17) and multiple experiments, gas friction is not a significant source of dissipation below 10 mTorr.

3.2.2.2 Surface losses

Surface losses are caused by adsorbed molecules, dangling or broken bonds, an amorphous oxide layer, or other metastable systems that occur at a resonator's surface. These systems absorb energy from the fundamental resonant mode and irreversibly transfer it other modes and thermal energy. For resonating beams, the energy of a resonator is stored in the elastic strain throughout its volume and thus is proportional to its volume, V. If we assume that energy is predominately dissipated at the surface, then we would expect that the energy lost per cycle would be proportional to the surface area S, and thus,

$$Q^{-1}_{\text{surface}} \propto \frac{S}{V} \propto L^{-1} \tag{3.18}$$

Fortunately, it may be possible to control surface losses (Jensen et al., 2006) in NEMS resonators, through careful experimental techniques and the proper choice of resonator material.

3.2.2.3 Clamping loss

Clamping loss refers to mechanical energy dissipated through the supports of a resonator. Typically, this is theoretically modeled as elastic radiation of energy through the supports. There is still some contention as to the appropriate description of elastic clamping loss, though the most recent theoretical calculations predict a loss for a rectangular beam of

$$Q^{-1}_{\text{clamping}} \propto \frac{wt^4}{l^5}, \tag{3.19}$$

where w is the beam width in the direction of vibration, t is the beam thickness, l is the beam length, and the proportionality constant is dependent upon material properties (Geller and Varley, 2005). Clearly, to reduce clamping loss, a beam with a high aspect ratio is desirable. However, according to Eq. (3.19), clamping loss should be negligible for current resonator designs, including nanotube resonators with their extremely high aspect ratio.

3.2.2.4 Thermoelastic loss

Thermoelastic damping is the result of the transformation of elastic energy into thermal energy via thermal currents flowing between compressed and expanded regions of a deformed resonator. Zener (1938) first studied the phenomenon for a beam in flexure, giving the damping as

$$Q^{-1}_{\text{Zener}} = \frac{E\alpha^2 T}{C_{\text{P}}} \frac{\omega\tau_0}{1+\omega^2\tau_0^2}, \tag{3.20}$$

where E is Young's modulus, α is the thermal expansion coefficient, C_{P} is the constant-stress heat capacity, ω is the angular frequency of vibration, T is temperature, and $\tau_0 = \frac{h^2 C_{\text{P}}}{\pi^2 K}$ is the thermal relaxation time, with K the thermal conductivity and h the beam thickness.

3.2.2.5 Ohmic loss

Another type of dissipation associated with electrostatic actuation is ohmic losses from the electrons moving on and off the resonator due to capacitive coupling to a nearby gate. Following Sazonova (2006), the system can be represented as a variable capacitor in series with a resistor to which a voltage V is applied. If the time scales for the electrons to flow on the resonator and the time for one oscillation are matched perfectly, all of the charge flows through a resistor, dissipating energy through Joule heating. Thus, the ohmic losses are given by

$$Q_{\text{Ohmic}}^{-1} = \frac{1}{\pi\omega}\frac{R(C'V)^2}{M_{\text{eff}}}, \tag{3.21}$$

where ω is the angular frequency of vibration, C' is the gradient of the capacitance, R is the output resistor and M_{eff} is the effective mass of the considered mode. The smaller the resonator, the smaller the mass, the higher this contribution, hence NEMS are very sensitive to this effect.

In nanomechanical resonators, there are other extrinsic loss mechanisms such as anharmonic mode coupling and extrinsic noise (Mohanty et al., 2002), which can be neglected compared to the other sources of dissipation already cited.

3.2.3 Thermomechanical Noise

Thanks to the fluctuation-dissipation theorem, it can be written that the force noise spectral density due to thermomechanical fluctuations of the mass is (Postma et al., 2005)

$$S_{\text{f}}(\omega) = \frac{2}{\pi}K_{\text{B}}T\frac{M_{\text{eff}}\omega_0}{Q}, \tag{3.22}$$

where M_{eff} is the effective mass of the resonator, ω_0 is the angular frequency of vibration, Q is the quality factor, K_{B} is Boltzmann's constant, and T is the resonator temperature.

It may be assumed without loss of generality that the bandwidth BW used by the phase locked loop (PLL) readout is very narrow compared with the −3dB bandwidth of the resonator. Then, following Eq. (3.14), the transfer function of the resonator at

resonance giving the displacement versus a constant force per unit length is

$$H_{\mathrm{fx}}(\omega)=\frac{Q}{K_{\mathrm{eff}}}=\frac{Q}{M_{\mathrm{eff}}\omega_0^2} \tag{3.23}$$

The displacement spectral density is then

$$S_{\mathrm{x}}(\omega_0)=S\left\|H_{\mathrm{fx}}(\omega)\right\|^2 S_{\mathrm{f}}(\omega)=\frac{2}{\pi}K_{\mathrm{B}}T\frac{Q}{M_{\mathrm{eff}}\omega_0^3} \tag{3.24}$$

Following Robins (1984), for a PLL-based readout technique, the frequency noise spectral density is

$$S_{\omega}(\omega)=\left(\frac{\omega_0}{2Q}\right)^2\frac{S_{\mathrm{x}}(\omega_0)}{P_0}, \tag{3.25}$$

where P_0 is the displacement carrier power, i.e., the RMS drive amplitude of the resonator $P_0 = \frac{1}{2}a_{\mathrm{d}}^2$. The latter should be driven below the hysteretic limit due to non-linearities. Even though this one will be higher when using a PLL-based technique, the open loop value may be used to stay on the safe side.

3.2.4 Resolution

The resolution is the lower limit of the dynamic range. It is set by the incoherent sum of all stochastic processes driving the resonator (Cleland and Roukes, 2002), such as thermomechanical fluctuations, quantum noise, noise from adsorption and desorption of gaseous species (Ekinci et al., 2004), and extrinsic sources such as vibrational and instrumental (read-out) noise. For simplicity, we solely consider thermomechanical noise in the case of a cantilever driven at its critical amplitude (open-loop stability limit). The resonator mass sensitivity (Eq. (3.11)) is

$$\mathrm{SF}_{\mathrm{m}}=\frac{1}{2M_{\mathrm{eff}}}f_0\propto l^{-3}\cdot t^{-1} \tag{3.26}$$

Thus, the mass sensor resolution is given by

$$\delta m=\frac{\sigma_{\omega}}{\mathrm{SF}_{\mathrm{m}}}\propto w^{-2}\cdot l^{7/2}\cdot t^{1/2} \tag{3.27}$$

At equilibrium, the concentration resolution for gas sensors is given by

$$\delta C = \frac{\delta m}{K_P V_P \rho_g} \propto w^{-3} \cdot l^{5/2} \cdot t^{1/2}, \tag{3.28}$$

where K_P is the partition coefficient depending on the couple polymer-gas combination, V_P is the polymer layer volume and ρ_g is the density of the gas analyte.

Equations (3.27) and (3.28) demand some important comments:

- In the case of resonant mass sensors, if the resonator dimensions are proportionally scaled down with respect to a given scale factor $N_{sf} << 1$, the resolution is proportionally improved with respect to N_{sf}^2. It proves that nanomechanical resonators, with their high fundamental resonance frequencies, diminished active masses and tolerable force constants, are extremely sensitive to mass changes. Therefore, for resonant mass sensors, NEMS resonators are a great alternative to improve the performances of such detectors.

$$\frac{\delta m(\text{NEMS})}{\delta m(\text{MEMS})} = N_{sf}^2 \tag{3.29}$$

- For resonant gas sensors, for a constant resonator width, if the resonator length and thickness are proportionally scaled down with respect to a given scale factor $N_{sf} << 1$ while keeping an acceptable slenderness ratio for Euler-Bernoulli beam model validity, the concentration resolution is proportionally improved with respect to N_{sf}^3. It proves that nanomechanical resonators are a great alternative for ultimate gas measurements.

3.2.5 Physical Nonlinearities

The validity of Eq. (3.1) is limited by the resonator physical nonlinearities. The mechanical nonlinearities are considered as a fundamental limit of the linear lower bound of the resonant sensor dynamic range (Cleland and Roukes, 2002). Furthermore, the actuation force can bring additional nonlinearities into the

resonator dynamics. Electrostatic actuation is a good example for spring softening nonlinearities (Kacem et al., 2009, 2010).

Nanoscale mechanical resonant sensors offer a greatly enhanced performance that is unattainable with microscale devices. However, scaling down resonators from MEMS to NEMS makes nonlinearities quickly reachable (Cleland and Roukes, 2002) and drastically alters the sensor resolution.

To underline this fact, let us write Eqs. (3.27) and (3.28) without restrictions on the displacement carrier power.

$$\delta m = \frac{\delta_\omega}{\mathrm{SF_m}} \propto w^{-1} \cdot l^{7/2} \cdot t^{1/2} \cdot a_\mathrm{d}^{-1} \cdot Q^{-1/2} \tag{3.30}$$

$$\delta C = \frac{\delta m}{K_\mathrm{p} V_\mathrm{p} \rho_\mathrm{g}} \propto w^{-2} \cdot l^{5/2} \cdot t^{1/2} \cdot a_\mathrm{d}^{-1} \cdot Q^{-1/2} \tag{3.31}$$

To simplify the analysis of Eqs. (3.30) and (3.31) when the resonator dimensions are scaled down, we suppose that the quality factor Q is constant. Then, it is clear that the resolution of nanomechanical resonators depends on the drive oscillation. The latter is limited by the mechanical nonlinearity for thin clamped-clamped resonators.

Under this limit, Eqs. (3.30) and (3.31) show that proportionally scaling down the resonator improves the sensor resolution. It is even more convenient to reduce only the beam length l and thickness t while keeping an acceptable slenderness ratio for the validity of the Euler-Bernoulli model. Ultimate optimization depends on the drive amplitude of the resonator. Ideally, the resonator should be actuated to oscillate at the highest possible amplitude (below the pull-in for an electrostatic actuation). In open loop, the resonator is classically driven below its critical amplitude in order to ensure the stability of its dynamic response. This fundamental limit is set by the nonlinear dynamics of the resonator (details are given in Sections 3.3 and 3.4).

However, when used as a practical sensor, the resonator is most of the time used as an oscillator, embedded in a feedback loop, or a PLL. In such closed-loop operation, the phase is the control parameter of the system (the frequency is now an output) and hence stabilizes its dynamics: even in the non-linear regime, the

frequency is a single valued function of the phase (Yurke et al., 1995; Juillard et al., 2008). In other words, the steady-state solution in the closed-loop case is always stable.

Now, the question is: What is the most important issue when the resonator is driven beyond its critical amplitude in either open or closed loop? The answer is detailed below.

3.2.6 Nonlinearities and Noise Mixing

In a capacitive resonator, mechanical and electrostatic nonlinearities are analytically combined to show that low-frequency voltage drift in the sustaining amplifier is directly converted into a frequency shift in the oscillator output. Experimental evidence of this effect is presented in Roessig et al. (1997), and it is shown that this is the dominant source of near-carrier frequency instability in tuning fork oscillators.

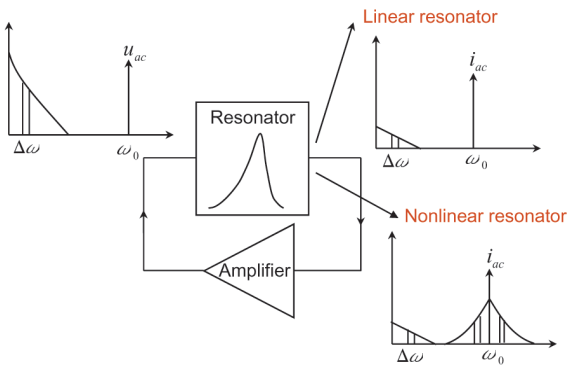

Figure 3.1 Schematic representation of noise aliasing in micro-oscillator. A linear resonator would filter out the amplifier low-frequency $\frac{1}{f}$-noise present at the resonator input, but nonlinear filtering element will result in noise aliasing (Kaajakari et al., 2005a).

Besides, a significant near-carrier noise source is the aliasing of $\frac{1}{f}$-noise to carrier side-bands due to the mixing of low-frequency noise and carrier signal in the active circuit elements. Kaajakari et al. (2005a) showed that, in addition to amplifier nonlinearities, the electrostatic transduction commonly used for coupling to

silicon resonators is inherently nonlinear and leads to aliasing of noise. This process is illustrated in Fig. 3.1, which shows a schematic representation of an oscillator comprising a resonator and sustaining amplifier. In addition to amplifying oscillation signal u_{ac}, the amplifier output may present a significant amount of low-frequency $\frac{1}{f}$-noise to the resonator input. A linear resonator element would effectively filter out this low-frequency noise, but nonlinearities in the resonator will lead to unwanted aliasing of the low-frequency noise to carrier side-bands. Thus, the capacitive coupling is expected to be intrinsically more prone to noise aliasing. A detailed analysis of the noise-mixing mechanisms can be found in Kaajakari et al., (2005a), where the capacitive force nonlinearity was found to be the dominant up-mixing mechanism in electrostatic transduction.

Since the capacitive transduction is commonly used for resonant nanocantilevers, any source of frequency instability in the oscillator is detrimental to the noise behavior of the transducer, so these sources must be understood and minimized or canceled.

Practically, in order to avoid most of noise, which reduces the resonant sensor performances, the resonator should be driven linearly beyond its fundamental critical amplitude. Therefore, for ultimate optimizations, one should investigate the open loop nonlinear dynamics of nanocantilevers.

3.3 Nanocantilever Based on Electrostatic Detection

In order to develop a model for micro/nanocantilever beams, a slender uniform flexible beam is considered as shown in Fig. 3.2. The beam is initially straight, and it is clamped at one end and free at the other end, subject to viscous damping with a coefficient $\tilde{c}$ per unit length and actuated by an electric load $v(t) = V_{dc} + V_{ac} \cos(\tilde{\Omega}\tilde{t})$, where V_{dc} is the DC polarization voltage, V_{ac} is the amplitude of the applied AC voltage, $\tilde{t}$ is time, and $\tilde{\Omega}$ is the excitation frequency. In addition, the beam follows the Euler–Bernoulli beam theory, where shear deformation and rotary inertia terms are negligible.

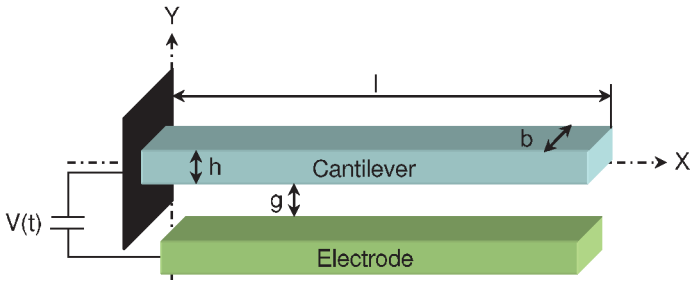

Figure 3.2 Schema of an electrostatically actuated nanocantilever.

3.3.1 Equation of Motion

Following a variational approach based on the extended Hamilton principle and used by Crespo da Silva and Glynn (1978b,d) and Crespo da Silva (1988a,b), the nonlinear equation of motion describing the flexural vibration of a cantilever beam electrostatically actuated can be written as

$$\begin{aligned} &EI\{\tilde{w}'''' + [\tilde{w}'(\tilde{w}'\tilde{w}'')']'\} + \rho bh\ddot{\tilde{w}} + \tilde{c}\dot{\tilde{w}} \\ &= -\frac{1}{2}\rho bh\left\{\tilde{w}'\int_l^s \left[\frac{\partial^2}{\partial \tilde{t}^2}\int_0^{s_1}(\tilde{w}')^2 ds_2\right] ds_1\right\}' \\ &\quad + \frac{1}{2}\varepsilon\frac{C_n b[V_{dc} + V_{ac}\cos(\tilde{\Omega}\tilde{t})]^2}{(g-\tilde{w})^2}, \end{aligned} \tag{3.32}$$

where primes and dots denote, respectively, the partial differentiation with respect to the arclength s and to the time $\tilde{t}$; $\tilde{w}$ is the beam bending deflection, E and I are Young's modulus and geometrical moment of inertia of the cross section, respectively; l and b are the length and width of the nanobeam, respectively; ρ is the material density; h is the nanobeam thickness in the direction of vibration; g is the capacitor gap width; and ε is the dielectric constant of the gap medium.

The first term in the left-hand side of Eq. (3.32) is due to the nonlinear expression for the curvature of the beam, while the first term in the right-hand side, which involves a double time derivative, is the nonlinear inertial term. The last term in Eq. (3.32) represents an approximation of the electrostatic force

assuming a complete overlap of the area of the nanobeam and the stationary electrode where C_n is the fringing field coefficient computed using an existing analytical model (Nishiyama and Nakamura, 1990). The boundary conditions are

$$\tilde{w}(0,\tilde{t}) = \tilde{w}'(0,\tilde{t}) = \tilde{w}''(l,\tilde{t}) = \tilde{w}'''(l,\tilde{t}) = 0 \tag{3.33}$$

3.3.2 Normalization

For convenience and equation simplicity, we introduce the nondimensional variables:

$$w = \frac{\tilde{w}}{g}, \quad x = \frac{s}{l}, \quad t = \frac{\tilde{t}}{\tau}, \tag{3.34}$$

where $\tau = \frac{2l^2}{h}\sqrt{\frac{3\rho}{E}}$. Substituting Eq. (3.34) into Eqs. (3.32) and (3.33), we obtain

$$\begin{aligned} &w^{iv} + \ddot{w} + c\dot{w} + \delta_1[w'(w'w'')']' \\ &\quad = -\delta^2\left\{w'\int_1^x\left[\frac{\partial^2}{\partial t^2}\int_1^{x_1}(w')^2\,dx_2\right]dx_1\right\}' \\ &\quad + d_3\frac{V_{dc}}{V_{ac}}\frac{[1+\frac{V_{ac}}{V_{dc}}\cos(\Omega t)]^2}{(1-w)^2} \end{aligned} \tag{3.35}$$

$$w(0,t) = w'(0,t) = w''(1,t) = w'''(1,t) = 0 \tag{3.36}$$

where primes and dots denote, respectively, the partial differentiation with respect to the dimensionless arclength x and to the dimensionless time t. The parameters appearing in Eq. (3.35) are

$$\begin{aligned} &c = \frac{\tilde{c}l^4}{EI\tau}, \quad \delta_1 = \left[\frac{g}{l}\right]^2, \quad \delta_2 = \frac{1}{2}\left[\frac{g}{l}\right]^2 \\ &\delta_3 = 6V_{ac}V_{dc}\frac{\varepsilon l^4}{Eh^3g^3}, \quad \Omega = \tilde{\Omega}\tau \end{aligned} \tag{3.37}$$

3.3.3 Solving

The beam total displacement $w(x, t)$ can be written as a sum of a static dc displacement $w_s(x)$ and a time-varying ac displacement

$w_d(x, t)$. However, for devices under low pressure, i.e., quality factors Q are in the range of 10^3 to 10^4, the static deflection is negligible with respect to the dynamic deflection.

A reduced-order model is generated by modal decomposition transforming Eq. (3.35) into a multi-degree-of-freedom system consisting of ordinary differential equations in time. We use the undamped linear mode shapes of the cantilever as basis functions in the Galerkin procedure. To this end, we express the deflection as

$$w(x,t) = \sum_{k=1}^{n} a_k(t)\phi_k(x), \tag{3.38}$$

where $a_k(t)$ is the k^{th} generalized coordinate and $\phi_k(x)$ is the k^{th} linear undamped mode shape of the straight microbeam, normalized such that $\int_0^1 \phi_k\phi_j = \delta_{kj}$ where $\delta_{kj} = 0$ if $k \neq j$ and $\delta_{kj} = 1$ if $k = j$. The linear undamped mode shapes $\phi_k(x)$ are governed by

$$\frac{d^4\phi_k(x)}{dx^4} = \lambda_k^2\phi_k(x) \tag{3.39}$$

$$\phi_k(0) = \phi_k'(0) = \phi_k''(0) = \phi_k'''(1), \tag{3.40}$$

Here, λ_k is the k^{th} natural frequency of the cantilever. The electrostatic force in Eq. (3.35) is expanded in a fifth order Taylor series in order to capture 5 possible amplitudes for a given frequency in the mixed behavior (Kacem and Hentz, 2009). Then, Eq. (3.38) is substituted into the resulting equation, Eq. (3.39) is used to eliminate $\frac{d^4\phi_k(x)}{dx^4}$, and the outcome is multiplied by ϕ_k and integrated from $x = 0$ to 1 for $k \in [1, n] \cap \mathbb{N}$. Thus, a system of coupled ordinary differential equations in time is obtained.

The DC voltage, which is generally at least ten times higher than the AC voltage, makes the second harmonic $\cos(2\Omega t)$ negligible with respect to the first harmonic $\cos(\Omega t)$. Also, assuming that the first mode is the dominant mode of the system, the study can be restricted to the case $n = 1$. Then, we obtain

$$40.44\delta_1 a_1^3 + 0.39\frac{V_{ac}}{V_{dc}}\delta_3 + 0.78\frac{V_{dc}}{V_{ac}}\delta_3 - \frac{V_{ac}}{V_{dc}}\delta_3 a_1 - 2\frac{V_{dc}}{V_{ac}}\delta_3 a_1 + 2.22\frac{V_{ac}}{V_{dc}}\delta_3 a_1^2 + 4.43\frac{V_{dc}}{V_{ac}}\delta_3 a_1^2$$

$$
\begin{aligned}
&-4.7\frac{V_{ac}}{V_{dc}}\delta_3 a_1^3 - 9.4\frac{V_{dc}}{V_{ac}}2\delta_3 a_1^3 + 9.75\frac{V_{ac}}{V_{dc}}\delta_3 a_1^4 \\
&+19.5\frac{V_{dc}}{V_{ac}}\delta_3 a_1^4 - 20\frac{V_{ac}}{V_{dc}}\delta_3 a_1^5 - 40\frac{V_{dc}}{V_{ac}}\delta_3 a_1^5 \\
&+a_1\lambda_1^2 + c\dot{a}_1 + 9.2\delta_2 a_1\dot{a}_1^2 + \ddot{a}_1 + 9.2a_1^2\delta_2\ddot{a}_1 \\
&+1.56\delta_3\cos(\Omega t) - 4\delta_3 a_1^3\cos(\Omega t) \\
&+9\delta_3 a_1^2\cos(\Omega t) - 19\delta_3 a_1^3\cos(\Omega t)
\end{aligned} \tag{3.41}
$$

We recognize in the Eq. (3.41) some canonical nonlinear terms such as the Duffing nonlinearity as well as the parametric excitation (Mathieu term). However, the presence of other high order nonlinearities makes the described system in Fig. 3.2 as a forced nonlinear cantilever under multifrequency parametric excitation. This kind of equation is not so frequently treated in the literature: It includes terms coming from mechanical and electrostatic nonlinearities.

To analyze the equation of motion (3.41), it is convenient to invoke perturbation techniques, which work well with the assumptions of "small" excitation and damping, typically valid in NEMS resonators. To simplify the perturbation approach, in this case the averaging method, a standard constrained coordinate transformation is introduced, as given by

$$a_1 = A(t)\cos[\Omega t + \beta(t)] \tag{3.42}$$

$$\dot{a}_1 = -A(t)\Omega\sin[\Omega t + \beta(t)] \tag{3.43}$$

$$\ddot{a}_1 = -A(t)\Omega^2\cos[\Omega t + \beta(t)] \tag{3.44}$$

$A(t)$ and $\beta(t)$ are slowly time-varying functions. In addition, since near-resonant behavior is the principal operating regime of the proposed system, a detuning parameter σ is introduced, as given by

$$\Omega = \omega_1 + \xi\sigma, \tag{3.45}$$

where $\omega_1 = \sqrt{\lambda_1^2 - \frac{V_{ac}}{V_{dc}}\delta_3 - 2\frac{V_{dc}}{V_{ac}}\delta_3}$ and ξ is the small non-dimensional bookkeeping parameter. Separating the resulting equations and averaging them over the period $\frac{2\pi}{\Omega}$ in the t-domain results in the

system's averaged equations in terms of amplitude A and phase β given by

$$\dot{A} = \frac{\xi\delta_3 \sin\beta}{\omega_1}(0.78 + 1.11A^2 + 2.44A^4) - \frac{\xi c}{2}A + O(\xi^2) \tag{3.46}$$

$$\begin{aligned}\dot{\beta} = {} & \sigma\xi - \xi\frac{\delta_3\cos\beta}{\omega_1}\left(\frac{0.78}{A} + 3.32A + 12.19A^3\right) \\ & + \xi\frac{A^4\delta_3}{\omega_1}\left(12.51\frac{V_{dc}}{V_{ac}} - 6.25\frac{V_{ac}}{V_{dc}}\right) - \xi\frac{15.16A^2\delta_1}{\omega_1} \\ & + \frac{\xi\delta_3 A^2}{\omega_1}\left(1.76\frac{V_{ac}}{V_{dc}} + 3.52\frac{V_{dc}}{V_{ac}}\right) + 2.3\xi A^2\delta_2\omega_1 + O(\xi^2)\end{aligned} \tag{3.47}$$

The steady-state motions occur when $\dot{A} = \dot{\beta} = 0$, which corresponds to the singular points of Eqs. (3.46) and (3.47). Thus, the frequency response equation can be written in its parametric form $A = K_1(\beta)$, $\Omega = K_2(\beta)$ as a function of the phase β. This set of two equations is easily implementable in Matlab or Mathematica. This ability makes the model suitable for NEMS designers as a quick tool to optimize the resonant sensors performance.

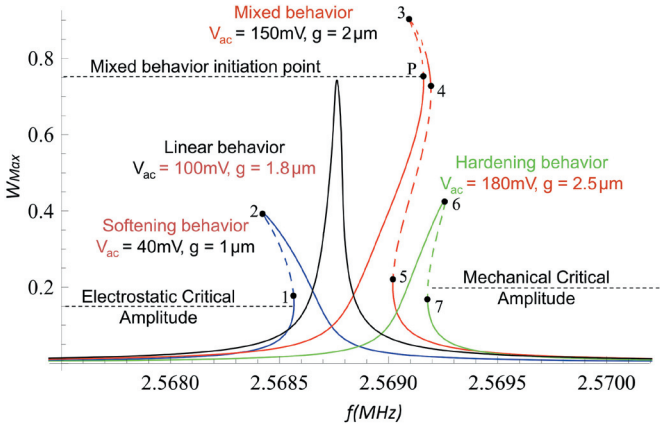

Figure 3.3 Analytical forced frequency responses for $Q = 10^4$ and several values of g and V_{ac}; W_{max} is the beam displacement at its free end normalized by the gap g, A_c is the critical amplitude above which bistability occurs, the different bifurcation points are {1, 2, 3, 4, 5, 6, 7, P}, the P point characterizes the initiation of the mixed behavior.

The plots of Fig. 3.3 were carried out with the following set of parameters: l = 12.5 μm, h = 300 nm, b = 500 nm, and V_{dc} = $50V_{ac}$; g and V_{ac} were used for parametric studies. This analytical model enables the capture of all the nonlinear regimes in the resonator dynamics and describes the competition between the mechanical hardening and the electrostatic softening behaviors. In addition, the model permits the optimization of the resonator design by tuning the geometrical parameters in order to cancel out nonlinearities as shown in Fig. 3.3. For g = 1.8 μm, V_{dc} = 5 V and $Q = \rho bh \frac{\omega_1}{\tau\tilde{c}} = 10^4$ (black curve). The obtained linear behavior enhances the detection limit of NEMS resonant sensors.

3.3.4 Critical Amplitude

The critical amplitude is the oscillation amplitude A_c above which bistability occurs. Thus, A_c is the transition amplitude from the linear to the nonlinear behavior.

3.3.4.1 The mechanical critical amplitude

By using Eqs. (3.46) and (3.47) when the mechanical nonlinearities (terms proportional to δ_1 or δ_2) are dominating the cantilever dynamics, the parametric form of the frequency response can be written as

$$\Omega = 1 + \zeta_0 \cot\beta + 0.077\delta_1\zeta_1^2 \sin^2\beta \tag{3.48}$$

$$A = 2\zeta_1 \sin\beta, \tag{3.49}$$

where ζ_0 = 0.142206c and $\zeta_1 = \frac{0.445\delta_3}{c}$.

Mathematically, A_{cm} is defined as the oscillation amplitude for which the equation $\frac{d\Omega}{d\beta}$ = 0 (infinite slope) has a unique solution $\beta_{cm} = \frac{\pi}{3}$. Thus, the critical electrostatic force is deduced as $\zeta_{1c} = \frac{0.456\sqrt{\zeta_0}}{\delta_1}$.

The critical amplitude A_{cm} is obtained by substituting the critical electrostatic force into Eq. (3.49) at the point $\beta = \frac{\pi}{2}$ and multiplying by the gap g and the value of the first linear undamped mode shape function ϕ_1 at the free point of the beam. Finally, we obtain the following close-form solution:

$$A_{\mathrm{cm}} = 6.3\frac{1}{\sqrt{Q}} \tag{3.50}$$

Remarkably, the mechanical critical amplitude of a resonant cantilever depends only on its length and its quality factor. However, for a clamped-clamped resonator, the mechanical critical amplitude is $A_{\mathrm{cm}} = 1.68\frac{h}{\sqrt{Q}}$ (Kacem et al., 2009); it depends only on the resonator width in the direction of vibration and its quality factor. For a given quality factor, the ratio between both critical amplitudes is $R_{\mathrm{c}} = \frac{A_{\mathrm{cm}}^{\mathrm{c\text{-}f}}}{A_{\mathrm{cm}}^{\mathrm{c\text{-}c}}} = 3.75\frac{l}{h} = 3.75\lambda_{\mathrm{e}}$, where λ_{e} is the slenderness ratio of the beam. While the resonator is sufficiently slender to validate the Euler–Bernoulli theory, the dynamic range ratio between cantilevers and clamped-clamped beams is very high (>20), which makes nanocantilevers an advantageous candidate for NEMS resonators-based applications.

3.3.4.2 The electrostatic critical amplitude

In this case, the electrostatic nonlinearities in Eqs. (3.46) and (3.47) are supposed to be dominating the cantilever dynamics. Considering only nonlinear terms up to the third order, while neglecting the parametric terms and the terms proportional to V_{ac}^2, the form of the frequency response can be written as

$$\Omega = \frac{c}{2}\cot\beta - \frac{8.64\frac{V_{\mathrm{dc}}}{V_{\mathrm{ac}}}\delta_3^3}{c^2\omega_1^3}\sin\beta^2 + \frac{6.2}{\omega_1} - \frac{V_{\mathrm{dc}}^2\delta_3}{\omega_1} + \frac{\omega_1}{2} \tag{3.51}$$

$$A = \frac{3.13\delta_3}{c\omega_1}\sin\beta \tag{3.52}$$

Mathematically, A_{ce} is defined as the oscillation amplitude for which the equation $\frac{d\Omega}{d\beta} = 0$ has a unique solution $\beta_{\mathrm{ce}} = \frac{\pi}{3}$. Thus, the critical electrostatic AC voltage is deduced as

$$V_{\mathrm{ac_c}} = 11.2V_{\mathrm{dc}}\frac{\delta_3^3}{c^3\omega_1^3} \tag{3.53}$$

The electrostatic critical amplitude A_{ce} is obtained by sub-stituting Eq. (3.53) into Eq. (3.52) at the pointt $\beta = \frac{\pi}{2}$ and multiplying by the gap g and the value of the first linear undamped mode shape function ϕ_1 at the free point of the beam.

$$A_{ce} = 2 \times 10^9 g^{\frac{5}{2}} \frac{h}{l\sqrt{Q}V_{dc}} \left(\frac{7.5 \times 10^7 h^2}{l^4} - \frac{3.8 \times 10^{-15} V_{dc}^2}{g^3 h} \right)^{\frac{1}{4}} \quad (3.54)$$

Unlike the mechanical critical amplitude (Eq. (3.50)), the electrostatic critical amplitude of a resonant cantilever depends on its length l, its width in the direction of vibration h, the gap g, the DC voltage as well as the quality factor Q.

3.3.4.3 Engineering optimization

The hysteresis suppression is based on the counterbalance between hardening mechanical nonlinearities and softening electrostatic nonlinearities. The mixed behavior, captured by including the fifth order nonlinear electrostatic terms, is less pronounced than in electrostatically driven clamped-clamped beams. Therefore, while neglecting the fifth order terms, the nonlinearity cancellation based on the critical amplitude expressions can be written as

$$A_{c_m} = A_{c_e} \quad (3.55)$$

Thus, assuming a constant quality factor Q, the optimal DC drive voltage is

$$V_{dc_{OP}} = \sqrt{\frac{1}{2}\sqrt{\frac{1.65 \times 10^{39} g^{14} h^6}{l^{16}} + \frac{3.2 \times 10^{42} g^{10} h^6}{l^{12}}} - \frac{8.1 \times 10^{19} g^7 h^3}{l^8}} \quad (3.56)$$

In reality, the overall quality factor may decrease when V_{dc} increases because of the ohmic losses from the electrons moving on and off the resonator due to capacitive coupling to a nearby electrode (Sazonova, 2006). This ohmic contribution adds up to the other sources of dissipation (thermomechanical, anchor losses, adsorption/desorption ...) like $Q_{total}^{-1} = Q_{thermo}^{-1} + Q_{anchor}^{-1} + \cdots + Q_{ohmic}^{-1}$ and may be expressed as $\left(Q_{ohmic}^{-1} = \frac{1}{\pi\omega} \frac{R(C'V_{dc})^2}{M_{eff}} \right)$, (Sazonova, 2006) where C' is the gradient of the capacitance, R is the output resistor and M_{eff} is the effective mass of the considered mode.

Then, the quality factor should be changed to $\frac{1}{Q^{-1} + Q_{ohmic}^{-1}}$, for the electrostatic critical amplitude and thus, the optimal DC drive voltage can be deduced using the same Eq. (3.55).

In the particular case of Fig. 3.3, the mechanical critical amplitude is A_{c_m} = 0.2 g. When g = 1.8 µm and for a quality factor $Q = 10^4$, the optimal DC drive voltage taking into account the ohmic losses, is around 5 V. At this voltage, as shown by the black curve of Fig. 3.3, the peak amplitude is linear and beyond the critical amplitude (A_{peak} = 0.8 g). Therefore, the enhancement $\left(\frac{A_{peak}}{A_c}\right)$ rate of the sensor performance is around 4.

Remarkably, the electrostatic critical amplitude is independent on the AC voltage. This is due to the use of a low AC voltage compared to the DC voltage for the cantilever actuation, which makes the contribution of V_{ac} in the electrostatic Duffing term negligible. Hence, in this configuration, the compensation of the nonlinearities is independent on the AC voltage. This interesting result makes possible the enhancement of the nanocantilever performances up to very high displacements comparable to the gap in the case of an electrostatic actuation by increasing the AC voltage, and limited by an upper bound instability such as the pull-in (Nayfeh et al., 2007).

The aim of this model is to provide practical analytical rules for MEMS and NEMS designers in order to optimize resonant sensor performances. Hence, it is important to check its validity experimentally on nanocantilever electrostatically actuated.

3.3.5 Fabrication

Practical applications of nanocantilever beams benefit much from on-chip signal processing, whereby optimal performance is achieved in case of monolithic integration with CMOS (Verd et al., 2006, 2008; Arcamone et al., 2008, 2007). Such NEMS/CMOS made of silicon combine unique sensing attributes, thanks to the high resonance frequency mobile mechanical part, with the possibility to electrically detect the output signal in enhanced conditions. For those reasons, the nanobeams that are experimentally studied in this work have been monolithically integrated with a dedicated CMOS circuit to enhance the capacitive readout of their resonance “motional” current. This heterogeneous integration has required a very specific fabrication process described hereafter. More details about the process and the functionality of this NEMS/CMOS system can be found in Arcamone et al. (2007, 2008).

The cantilevers fabrication process used here has been performed at CNM-IMB (CSIC) in Barcelona (Spain) and at EPFL in Lausanne (Switzerland). It is based on a post-processing approach in which CMOS circuits are first fabricated according to a standard CMOS technology, then NEMS resonators are subsequently patterned by nanostencil lithography (nSL) (van den Boogaart et al., 2004) and fully fabricated. nSL is a shadow-mask based, full-wafer and parallel nanopatterning technique providing a resolution down to 200 nm and a high fabrication throughput.

After concluding the fabrication of the CMOS circuits, dedicated areas (located close to each circuit, 1 per circuit) are selectively patterned with an 80 nm thick aluminum layer by nSL. The following step is a reactive ion etching (RIE) of silicon that transfers the aluminum patterns to the polysilicon structural layer of the resonators. The last step consists in releasing the resonators and removing the Al mask by a local wet etching based on HF acid. The circuit is robustly protected during this etching by an adequately annealed photoresist layer. This entire process is described in Arcamone et al. (2008).

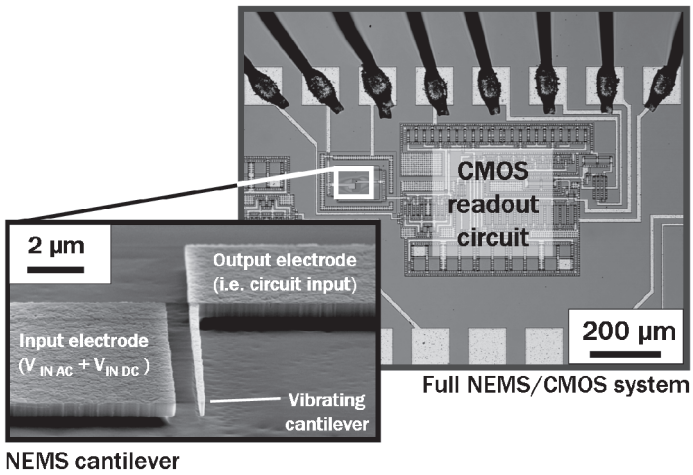

Figure 3.4 Optical picture of the NEMS resonator/CMOS readout circuit system. The scanning electron micrograph zooms the cantilever beam itself and its driving electrode.

CMOS wafers containing each 2000 fully fabricated nanomechanical devices of diverse types have been obtained with that

process; all connected to dedicated CMOS circuits for signal interfacing and amplification. Figure 3.4 depicts a fully fabricated nanocantilever beam (optimized for in-plane motion) which is monolithically integrated with its dedicated CMOS readout circuit.

3.3.6 Electrical Characterization

Electrostatic actuation and capacitive detection are used for detecting in-plane oscillations (in the MHz range) of those Si nanocantilever resonators. When the resonator is electrostatically driven by a DC + AC voltage, the readout electrode (i.e. the cantilever itself in our case, see Fig. 3.4), electrically connected to the closely located CMOS circuit input, collects a capacitive current in enhanced conditions since parasitic capacitances at the NEMS output are drastically reduced to the few fF range. The motional current I_{M}, which is a fraction of the total NEMS output current I_{MEMS}, is specifically generated by the variation of electrode/resonator capacitance due to the mechanical motion itself. The other part, the background current I_{BG}, is related to the capacitive feed through between the NEMS input and output electrodes, one part of it being the "static" capacitance between the cantilever and the in-front electrode, the other part being the parasitic fringing capacitance between both.

The dedicated CMOS readout circuit ensures a constant voltage biasing at the resonator output, while it amplifies the readout current by a factor 100 and converts it to an output voltage according to an external load resistor R_{LOAD} (see Fig. 3.5). Arcamone et al. (2007, 2008) give more details on the circuitry and the readout scheme.

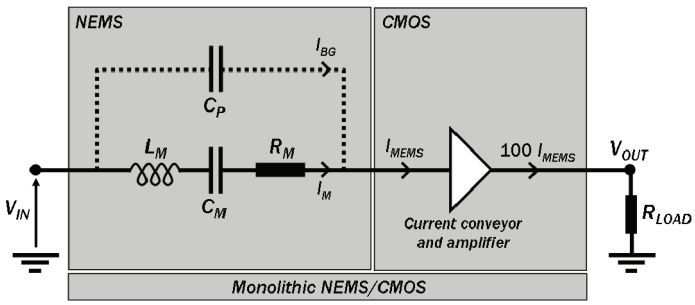

Figure 3.5 Electrical scheme of the monolithic NEMS/CMOS system.

The mechanical frequency response of those nanocantilevers has been electrically characterized with a network analyzer (AGILENT E5100A) in air (with a probe station) and vacuum (with wire-bonded samples). In both configurations, the capacitive detection scheme including the CMOS circuit successfully transduced into an electrical signal the mechanical motion corresponding to the fundamental in-plane flexural resonance mode of vibrating cantilevers. The data collected by the network analyzer, in terms of magnitude and phase, are under the following form:

$$R_{\mathrm{NA}}(f) = 20\log\frac{V_{\mathrm{OUT\,AC}}}{V_{\mathrm{IN\,AC}}} \tag{3.57}$$

The NEMS resonator total current (at the cantilever output, not at the circuit output) being

$$I_{\mathrm{BG}} + I_{\mathrm{M}} = I_{\mathrm{MEMS}} = \frac{V_{\mathrm{IN\,AC}}}{100R_{\mathrm{LOAD}}} 10^{\frac{R_{\mathrm{NA}}}{20}} \tag{3.58}$$

The modulus and argument of the NEMS resonator electrical admittance Y can be calculated based on the circuit characteristics and the network analyzer response as follows:

$$|Y| \approx \frac{I_{\mathrm{MEMS}}}{V_{\mathrm{IN\,AC}}} = \frac{10^{\frac{R_{\mathrm{NA}}}{20}}}{100R_{\mathrm{LOAD}}} \tag{3.59}$$

$$\arg(Y) = P - \Delta\phi, \tag{3.60}$$

where P is the phase signal as measured by the network analyzer and $\Delta\phi$ is the phase delay introduced by the circuit; in our case $\Delta\phi \approx \frac{\pi}{4}$. In the 2-port configuration of these measurements, a NEMS cantilever can be modeled as two parallel branches (see Fig. 3.5):

- a capacitive branch (of capacitance C_{P}), of admittance Y_{BG}, corresponding to the background signal, in which I_{BG} flows. Y_{BG} is given by $Y_{\mathrm{BG}} = sC_{\mathrm{P}}$ with $s = j\omega$.
- an RLC branch of admittance Y_{M}, corresponding to the resonating part, in which I_{M} flows. Y_{M} is given by $Y_{\mathrm{M}} = \dfrac{Cs}{LCs^2 + RCs + 1}$

The total admittance is then $Y = Y_{BG} + Y_M$. The theoretical model described in the previous section is expressed in terms of Y_M only, i.e., the term describing the oscillations. Therefore, it is required to apply a simple data treatment to extract the motional admittance Y_M from the measured admittance Y, Y_M being given by $Y_M = Y - Y_{BG} = Y - sC_P$. Hence, its modulus is given by

$$|Y_M| = \sqrt{[|Y|\cos(\arg(Y))]^2 + [|Y|\sin(\arg(Y)) - \omega C_P]^2} \tag{3.61}$$

C_P can be estimated by considering the electrical response R_{NA-OOR} at a given frequency f_{OOR} that is out of resonance, then C_P is given by

$$C_P = \frac{1}{2\pi f_{OOR}} \frac{10^{\frac{R_{NA-OOR}}{20}}}{100 R_{LOAD}} \tag{3.62}$$

Figure 3.6a shows the raw electrical response R_{NA} around the mechanical resonance of cantilever A (l = 14.5 µm, b = 460 nm, h = 400 nm, g = 600 nm) as directly measured by the network analyzer. Figure 3.6b shows the motional admittance Y_M extracted from the data of Fig. 3.6a according to Eq. (3.61). Using the developed model, the motional admittance can be computed as follows:

$$I_M = Y_M V_{ac} = \frac{dC_{res}}{dt} V_{dc} \tag{3.63}$$

$$\frac{dC_{res}}{dt} = \int_0^1 \frac{bC_n \varepsilon_0 \phi_1(x) \dot{a}_1(t)}{(1 - a_1)(t) \phi_1(x))^2} dx \tag{3.64}$$

The derivative of the resonator capacitance with respect to the dimensionless time t has been expanded in a fifth order Taylor series, which enables the analytical computation of the integral in Eq. (3.64). Then, Eqs. (3.42) and (3.43) are substituted into the outcome equation and the trigonometric functions are linearized. Since the electrical measurement filters out all frequency components of the readout signal except which of the drive frequency, the first harmonic of the Fourier transform of Eq. (3.63) gives the motional current frequency response including the coupling between the dynamics of the resonator and the read-out voltage Eq. (3.64). Although this coupling brings

extra nonlinear terms, their contribution happens to be negligible and the read-out voltage is proportional to the dynamic deflection.

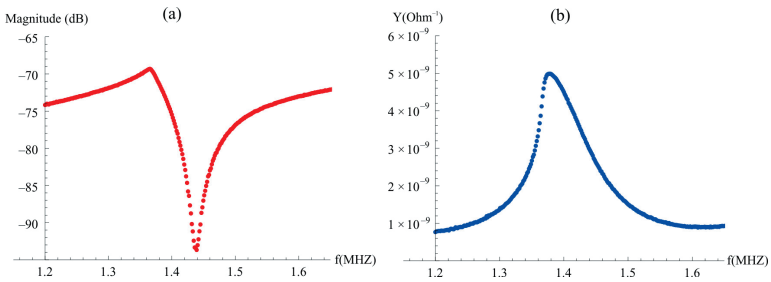

Figure 3.6 (a) Raw electrical response R_{NA} around the mechanical resonance of a nanocantilever. This is the response as measured by the NA of the full NEMS-CMOS system. (b) Motional admittance frequency response extracted from the data of Fig. 3.6a according to Eq. (3.61).

3.3.6.1 Measurements in air

It is important to underline that all the inputs of the model are known physical parameters including the fringing field coefficients computed using the analytical formulae (Nishiyama and Nakamura, 1990), except the measured quality factor Q and the parasitic capacitance C_P. Therefore, to evaluate the model, Q has been fitted using linear curves. For a fully analytical prediction, the quality factor may be computed using existing models taking into account the thermoelastic damping (Lifshitz and Roukes, 2000), the support loss (Hao et al., 2003), and the surface loss (Yang et al., 2002). Such a computation gives results in good agreement with experimental measurements.

Figure 3.7 shows the characteristic responses analytically computed and electrically measured of cantilever A (l = 14.5 μm, b = 460 nm, h = 400 nm, g = 600 nm) operated in air for several DC voltages. Due to some mass that has been deposited at the free end of the cantilever, its resonance frequency was shifted from 2 MHz down to 1.5 MHz. The first linear curve (V_{dc} = 16V) is fitted by adjusting the parasitic capacitance C_P and the quality factor Q. Then, the same value of C_P has been used for the three other curves while adjusting the Q factor for each one.

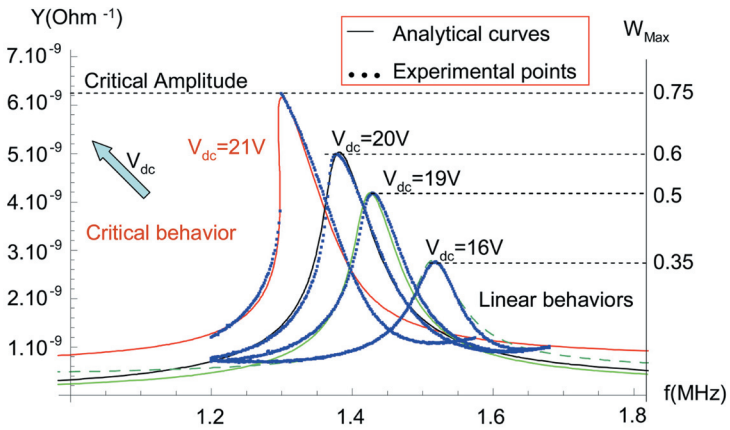

Figure 3.7 Analytical and measured motional admittance frequency curves (in air) of cantilever A. W_{max} is the cantilever displacement at its free end normalized by the gap.

Figure 3.7 shows that the resonance frequency of the cantilever can be tuned by varying the applied DC voltage and a clear spring-softening effect is seen with increasing V_{dc}. The analytical curves are in good agreement with experimental results and the critical amplitude predicted analytically for a 21 V DC voltage has been experimentally confirmed as shown in Fig. 3.7. which demonstrates the accuracy and performance of the model. Out of resonance, the experimental curves slightly increase which is due to the variation of $\Delta\phi$ during the measurements.

When experiments are performed in air, in order to reach detectable signals, the applied DC voltage has to be high ($V_{dc} > 10$ V). As the quality factor is low ($15 < Q < 20$), the dynamic behavior of the nanocantilever is dominated by the nonlinear softening electrostatic forces which significantly increases the critical amplitude Eq. (3.54).

3.3.6.2 Measurements in vacuum

The chip containing cantilever *B* ($l = 14.5$ µm, $b = 570$ nm, $h = 260$ nm, $g = 820$ nm) has been wire bonded and it has been measured in a vacuum chamber under a pressure of 10^{-2} mBar. The fits have been made in the same way as for the experimental curves

measured in air. Figure 3.8 shows two measured frequency responses and their predicted analytical curves.

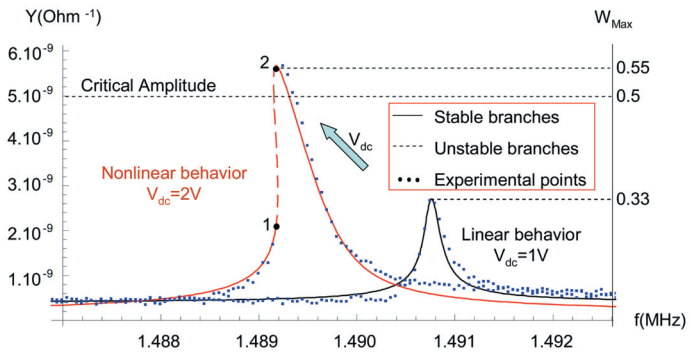

Figure 3.8 Analytical and measured motional admittance frequency curves (in vacuum) of cantilever B. $W_{\max}$ is the cantilever displacement at its free end normalized by the gap.

Due to the high quality factors obtained in vacuum, low drive voltages are enough to polarize the device: 1 or 2V DC added to a 0.092V AC. A 2V DC polarization is sufficient to provoke a nonlinear behavior yielding almost vertical slopes both in magnitude and in phase. The extracted Q factor decreases from 9150 down to 6650 for 1 and 2V DC polarization due to the ohmic losses (Sazonova, 2006).

The high quality factors reduce the critical amplitude A_c as shown in Fig. 3.8, which confirms the accuracy of the model beyond the critical amplitude (second curve with 2V DC). The effect of the spring softening is also present due to the electrostatic negative stiffness. Even with high quality factors, the cantilever B displays a softening behavior. This can be explained by the fact that the nonlinearities coming from the electrostatic force are stronger than the mechanical hardening nonlinearities due to the length of the beam and the small gap thickness.

In air, NEMS cantilever have a large critical amplitude (75% of the gap as shown in Fig. 3.7 for cantilever A) which implies a large dynamic range compared to clamped-clamped NEMS resonators (their critical amplitude could be lower than 1% of the gap). In addition, even in vacuum with high quality factors, the critical amplitude of nanocantilevers still interestingly large (50% of the

gap as shown in Fig. 3.8 for cantilever B). This important property makes cantilevers the best candidates for resonant mass and gas sensing devices.

The electric characterization of the NEMS/CMOS devices earlier described was an important step towards the validation of the nonlinear model for NEMS cantilevers. As previously shown, the competition between both behaviors (softening and hardening) is controlled by the design parameters, the quality factor as well as the DC voltage. The model shows that for appropriate values of those parameters, it is possible to suppress the hysteresis and to obtain an optimal design for which the mechanical and the electrostatic nonlinearities would be equilibrated. The next step is the complete validation of the model through the compensation of the nonlinearities, which is the subject of the next section.

3.4 Nanocantilever Based on Piezoresistive Detection

3.4.1 Device Description

The device is composed of a fixed-free lever beam and two piezoresistive gauges connected to the cantilever at a distance $d = 0.15l$ from its fixed end. This value was chosen to maximize the stress inside the gauges due to the cantilever motion (Fig. 3.9). The gauges have been etched along the <110> direction in order to benefit from the high gauge factor associated with p^{++} doped silicon. A driving electrode was patterned along one side of the resonant cantilever for electrostatic actuation. The NEMS cantilever is actuated electrostatically at the primary resonance of its first linear undamped mode shape. The cantilever oscillation induces stress inside the piezoresistive gauges and the collected strain is transduced into a resistance variation due to the piezoresistive effect. Thus, the sensor frequency response is obtained via a piezoresistive read-out perfectly decoupled from the capacitive actuation of the resonator. The amount of molecules absorbed by the functionalized surface of the cantilever changes its effective mass, which lowers its frequency resonance. By evaluating the frequency shift, the mass of the added species can be estimated.

Thus, the considered device can be used as either a mass or a gas sensor.

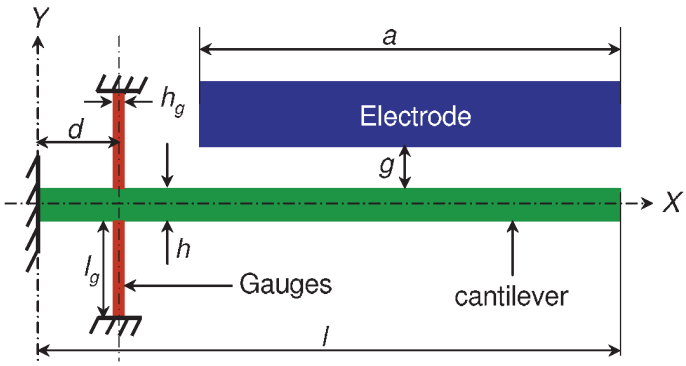

Figure 3.9 Resonant nanocantilever based on piezoresistive detection.

3.4.2 Transduction

The cantilever motion is detected by using the piezoresistive transduction principle (Mo Li and Roukes, 2007). The piezoresistive transducers consist on semiconducting silicon *p*++ (boron) doped suspended nanogauges. The rationale for using piezoresistive doped silicon nanogauges is related to the giant piezoresistance effect of these materials appearing for sub-100 nm dimensions (He and Yang, 2006). They are suitable for integrated transducers and for self-sensing devices (Arlett et al., 2006). The figure of merit characterizing these materials is the piezoresistive gauge factor γ defined as

$$\gamma = (1+\nu) + \frac{1}{\varepsilon_l}\frac{\Delta\rho}{\rho}, \tag{3.65}$$

where ρ is the resistivity, ε_l the gauge elongation and ν the Poisson ratio. The gauge factor relates the mechanical strain applied on the gauges to its relative resistance change. The resistance change depends on two effects. The first term in Eq. (3.65) is a geometrical consequence and is associated with elastic deformation, while the latter is related to the modification of the energy bands inside a crystal and thus altering its resistivity. In metals only the first term participates which ranges from 1–2 and is the way chosen by Roukes et al. (Yang, 2006). In semiconductors, the

second term provides a significant contribution, which was shown to be more than three orders of magnitude higher (He and Yang, 2006). The force applied to the lever is amplified by the appropriate design and transferred to the gauges. This design makes possible to exploit a first order piezoresistance effect with the suspended gauges acting as strain collectors instead of second order one (He et al., 2008). We should notice that there is no need for further metallization layers, which lead to additional damping and energy dissipation. The strain collected by the gauges is transduced into a resistance variation due to the piezoresistance effect proportional to

$$\frac{\Delta R(\Omega)}{R} = \gamma \varepsilon_1(\Omega) \tag{3.66}$$

3.4.3 Equation of Motion

The nonlinear equations of motion describing the flexural vibration of the device described in Fig. 3.9 can be derived using the extended Hamilton principle (Silva and Glynn, 1978b,d; Silva, 1988a,b). The cantilever bending deflection $\tilde{w}_j$ is decomposed into $\tilde{w}_0$ for $\tilde{s} \in [0, d]$ and $\tilde{w}_1$ for $\tilde{s} \in [d, l]$.

$$\begin{aligned} E_c I_c &= \{\tilde{w}_j'''' + [\tilde{w}_j'(\tilde{w}_j'\tilde{w}_j'')']'\} + \rho bh\ddot{\tilde{w}}_j + \tilde{c}\dot{\tilde{w}}_j \\ &= -\frac{1}{2}\rho bh\left\{\tilde{w}_j' \int_{(1-j)d+jl}^{s} \left[\frac{\partial^2}{\partial \tilde{t}^2}\int_{jd}^{s_1}(\tilde{w}_j')^2 ds_2\right] ds_1\right\}' \\ &\quad + \frac{j}{2}\varepsilon \frac{C_n b[V_{dc} + V_{ac}\cos(\tilde{\Omega}\tilde{t})]^2}{(g - \tilde{w}_j)^2} H(S + a - 1) \end{aligned} \tag{3.67}$$

where s is the arclength; E_c and I_c are Young's modulus and moment of inertia of the nanocantilever cross section, respectively; l and h are the length and width of the nanobeam, respectively; b is the device thickness; ρ is the material density; g is the capacitor gap width; and ε is the dielectric constant of the gap medium. The last term in Eq. (3.67) represents an approximation of the electrostatic force assuming a partial distribution along the nanobeam length. H is a Heaviside function and C_n is the fringing field coefficient. The boundary conditions are

$$\tilde{w}_0 = (0,\tilde{t}) = \tilde{w}_0'(0,\tilde{t}) = \tilde{w}_1''(l,\tilde{t}) = \tilde{w}_1'''(l,\tilde{t}) = 0 \tag{3.68}$$

$$\tilde{w}_0(d,t) - \tilde{w}_1(d,\tilde{t}) = \tilde{w}_0'(d,\tilde{t}) - \tilde{w}_1'(d,\tilde{t}) = 0 \tag{3.69}$$

$$\tilde{w}_0''(d,\tilde{t}) - \tilde{w}_1''(d,\tilde{t}) = -\frac{I_g}{I_c l_g}\tilde{w}_0'(d,\tilde{t}) \tag{3.70}$$

$$\tilde{w}_0'''(d,\tilde{t}) - \tilde{w}_1'''(d,\tilde{t}) = -\frac{2h_g b}{I_c l_g}\tilde{w}_0'(d,\tilde{t}), \tag{3.71}$$

where $\tilde{t}$ is time, h_g and I_g are the width and the moment of inertia of the gauge cross section. Equations (3.70) and (3.71) are obtained by writing the force and torque moment equilibrium equations at the point $s = d$.

$$T_{sc}|_d + 2T_{ag}|_d = EI_c[\tilde{w}_0'''(d,\tilde{t}) - \tilde{w}_1'''(d,\tilde{t})] + 2Ebh_g\frac{\tilde{w}_0(d,\tilde{t})}{l_g} = 0 \tag{3.72}$$

$$M_{bc}|_d + M_g|_d = EI_c[\tilde{w}_0''(d,\tilde{t}) - \tilde{w}_1''(d,\tilde{t})] - EI_g\frac{\tilde{w}_0'(d,\tilde{t})}{l_g} = 0, \tag{3.73}$$

where T_{sc} is the shear force applied to the cantilever, M_{bc} is its bending moment, T_{ag} is the axial force applied to the gauges, and M_g is its corresponding torque moment.

3.4.4 Normalization and Solving

Similarly to the cantilever model presented in Section 3.3, we introduce the same nondimensional variables. Then, a reduced-order model is generated by modal decomposition (Eq. (3.38)) transforming the normalized equation of motion into a multidegree-of-freedom system consisting in ordinary differential equations in time. The undamped linear mode shapes, which are defined as piecewise functions for the device described in Fig. 3.10, are used as basis functions in the Galerkin procedure.

The electrostatic force is expanded in a fifth order Taylor series, and Eq. (3.38) is substituted into the resulting equation. Then,

Eq. (3.39) is used to eliminate $\frac{d^4\phi_k(x)}{dx^4}$, and the outcome is multiplied by ϕ_k and integrated from $x = 0$ to 1 for $k \in [1, n] \cap \mathbb{N}$. Thus, a system of coupled ordinary differential equations in time is obtained.

Figure 3.10 shows that between the clamped end of the cantilever and the gauges, the vibrations of the sensor are relatively negligible with respect to its dynamics between the gauges and the free end of the cantilever for the first four modes. Consequently, the nonlinear coupling between the mode shapes is negligible for $x \in [0, d]$ and when the sensor is actuated on its first mode, its dynamics can be approximated by the dynamics of a cantilever of length $l - d$.

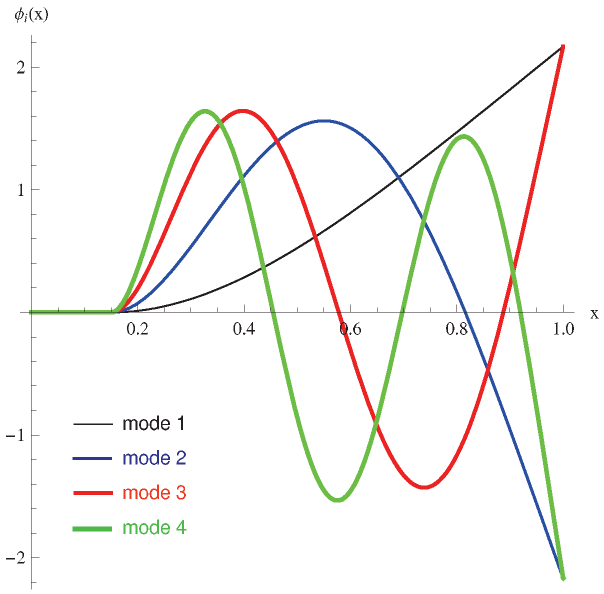

Figure 3.10 The first four linear undamped mode shapes of the device described in Fig. 3.9.

Assuming that the first mode is the dominant mode of the system, the study can be restricted to the case $n = 1$, which results in a nonlinear Mathieu-Duffing Equation. It can be solved using a perturbation technique which permits the transformation of the nonlinear second order equation into two first order nonlinear ordinary differential equation that describe the amplitude and phase modulation of the system frequency response. For

$V_{ac} << V_{dc}$, the second harmonic terms are neglected. The resulting phase and amplitude averaged equations over the period $\frac{2\pi}{\Omega}$ and around the primary resonance ($\Omega = \lambda_1 + \xi\sigma$) are

$$\dot{A} = f_1(A, \beta) \tag{3.74}$$

$$\dot{\beta} = f_2(A, \beta) \tag{3.75}$$

The steady-state motions occur when $\dot{A} = \dot{\beta} = 0$, which corresponds to the singular points of Eqs. (3.74) and (3.75). The normalized displacement W_{max} with respect to the gap at the free end of the cantilever and the drive frequency Ω can be expressed in function of the phase β. Thus, the frequency response curve can be plotted parametrically as shown in Fig. 3.11 for the following parameters: $l = 5$ µm, $b = 160$ nm, $h = 300$ nm, $l_g = 500$ nm, $h_g = 80$ nm, $a = 350$ nm and $V_{ac} = 0.1V_{dc}$. The gap g and the DC voltage V_{dc} were used for parametric studies.

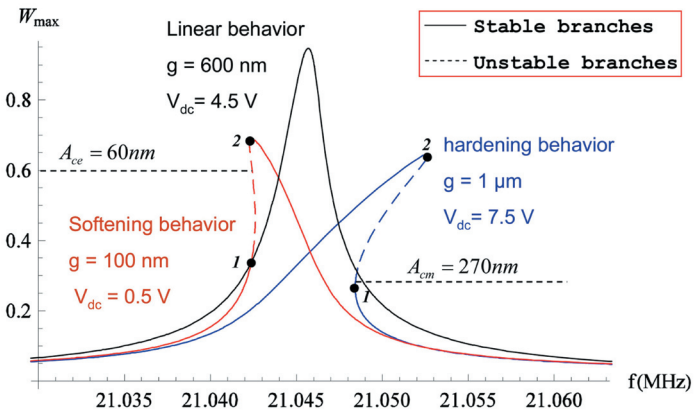

Figure 3.11 Analytical forced frequency responses of the resonant piezoresistive device presented in Figs. 3.9 and 3.12 for a quality factor $Q = 10^4$. W_{max} is the displacement of the beam normalized by the gap g at its free end.

3.4.5 The Critical Amplitude

3.4.5.1 The critical mechanical amplitude

The nonlinearities acting between the fixed end of the cantilever and the nanogauges are negligible since the vibration amplitudes

of this part are close to zero for the first linear undamped mode shape as shown in Fig. 3.10. Therefore, the NEMS behaves dynamically as a resonant nanocantilever of length $l - d$. Hence, using Eq. (3.50), the critical mechanical amplitude can be written as

$$A_{\mathrm{cm}} = 6.3\frac{l-d}{\sqrt{Q}} \tag{3.76}$$

3.4.5.2 The critical electrostatic amplitude

In this case, the mechanical nonlinearities are neglected. Also, the electrostatic nonlinearities are acting only on the sensor part comprised between the gauges and the free end of the cantilever. By considering only nonlinear terms up to the third order, while neglecting the parametric terms and the terms proportional to V_{ac}^2 and following Eq. (3.54), the critical electrostatic amplitude can be expressed as

$$A_{\mathrm{ce}} = \frac{2\times 10^9 hg^{5/2}}{(l-d)\sqrt{Q}V_{\mathrm{dc}}}\left(\frac{7.5\times 10^7 h^2}{(l-d)^4} - \frac{3.8\times 10^{-15}V_{\mathrm{dc}}^2}{g^3 h}\right)^{1/4} \tag{3.77}$$

3.4.5.3 Engineering optimization

As shown in Fig. 3.11, when $g << h$, the mechanical nonlinearities are negligible with respect to the electrostatic nonlinearities. Then, the NEMS forced frequency curve displays a softening behavior (red curve of Fig. 3.11) and the critical amplitude is given by Eq. (3.77), which depends on the quality factor Q, the cantilever width h, the gap g, the DC voltage V_{dc} and the distance $l - d$ between the piezoresistive nanogauges and free end of the cantilever. In this case, the open-loop stability of the NEMS resonant sensor is limited by an oscillation amplitude around 60 nm.

If $g >> h$, the electrostatic nonlinearities are negligible with respect to the mechanical nonlinearities. Then, the NEMS forced frequency curve displays a hardening behavior (blue curve of Fig. 3.11) and the critical amplitude is given by Eq. (3.76) which only depends on the quality factor Q and the distance $l - d$. In this case, the open-loop stability of the NEMS resonant sensor is limited by an oscillation amplitude around 270 nm: more than four times higher than the previous case. Thus, the mass resolution is enhanced by a factor $\Pi_{\mathrm{enh}} = 4$ compared to the first case.

Hence, designing NEMS cantilevers displaying a softening behavior is disadvantageous and can significantly alter the sensor resolution especially when this supposes that we are able to fabricate structures with very small gaps, which is rather awkward. Indeed, assuming that the upper bound limit (the pull-in) occurs at an amplitude of the gap order, even if the cantilever can vibrate linearly up to very high amplitudes comparable to the gap, the sensor performances can be altered due to its small dimensional amplitude limited by the gap. In other words, enhancing the dimensionless critical amplitude (red curve of Fig. 3.11) is not important when the gap is significantly reduced.

The optimal gap is g_p = 600 nm for which the mechanical and the electrostatic nonlinearities are balanced which permits the linearization of the frequency response as shown in Fig. 3.11 (black curve). For this design, which is technologically feasible, the mass resolution is enhanced by a factor Π_{enh} = 9, compared to first case.

3.4.6 Fabrication

The NEMS device presented in Fig. 3.12 was fabricated in CEALETI clean rooms using CMOS compatible materials with nano-electronics state-of-the-art lithography and etching techniques. A 200 mm silicon-on-insulator (SOI) wafer of <100> orientation was used. It comprises a 160 nm-thick top silicon structural layer (resistivity ≈ 10 Ωcm) and a 400 nm-thick sacrificial oxide layer. The top silicon layer was implanted with boron ions (p-type) through a thin layer of thermal oxide. Homogenous doping (3×10^{19} cm^{-3}) in the whole thickness of the top silicon was obtained through specific annealing step (for material reconstruction and doping activation), resulting in top layer resistivity of approximately 6 mΩcm. A hybrid e-beam/DUV lithography technique (Colinet et al., 2009) was used to define the nanoresonators and electrode pads, respectively. Top silicon layer was etched by anisotropic RIE. In order to decrease the lead resistances, the interconnecting leads have been thickened with a 650 nm thick AlSi layer, a typical metal for CMOS interconnection process. Finally, the nanoresonators have been released using a vapor HF isotropic etching to remove the sacrificial layer oxide beneath the structures. The main process steps are summarized in Fig. 3.13.

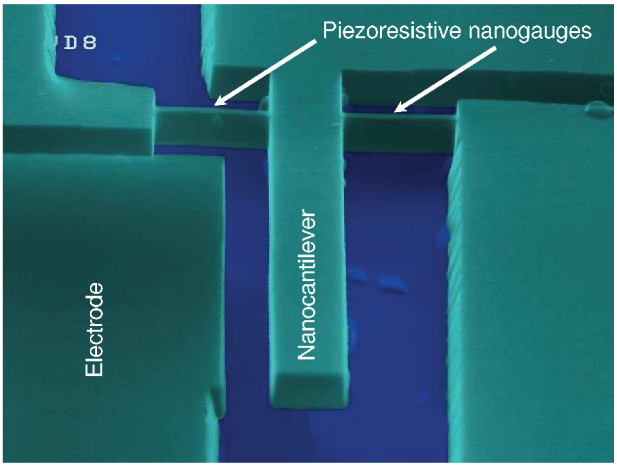

Figure 3.12 SEM image of the in-plane piezoresistive structure.

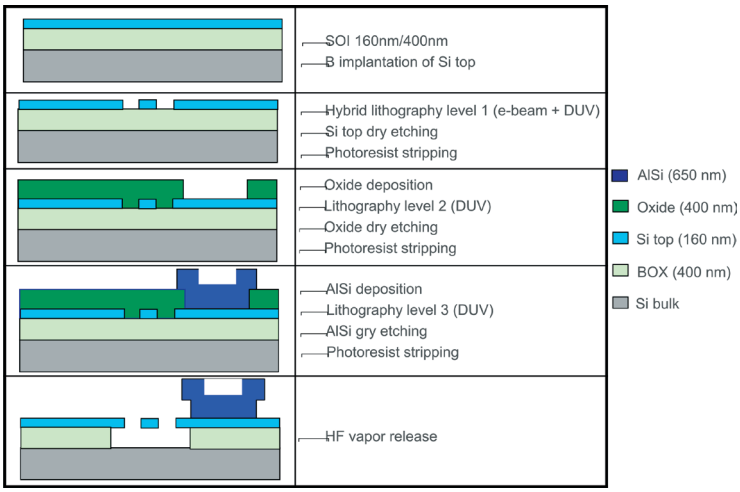

Figure 3.13 In-plane piezoresistive structure process flow.

3.4.7 Electrical Characterization

The strain collected by the gauges is transduced into a resistance variation due to the piezoresistance effect proportional to

$$\frac{\Delta R(\Omega)}{R} = \gamma \varepsilon_1(\Omega) = \gamma \frac{1}{24} l^3 h_g^2 g E[\phi_{11}'''(d) - \phi_{01}'''(d)] a_1(\Omega) \tag{3.78}$$

where R is the gauge resistance and E Young's modulus. The displacement frequency response $a_1(\Omega)$ can be written in its parametric form in order to plot parametrically the resistance frequency response with respect to the phase β.

3.4.7.1 ω Down-mixing technique

The devices under test were connected to a radio frequency (RF) circuit board through wire bonding and loaded to a RF vacuum chamber for room temperature measurements. The beam is actuated electrostatically through capacitive coupling and detected through piezoresistive displacement transduction. The electrical read-out at high frequency is complicated by parasitic capacitances, which change the expected behavior of the electrical circuit. In order to avoid parasitic impedances and to easily reach the nonlinear regime, an ω down-mixing technique has been used to read-out the resistance variation at a lower frequency $\Delta\omega$ (Bargatin et al., 2005) (a schematic of the setup is shown in Fig. 3.14). The change in resistance $\Delta R(\omega)$ is read by applying a proper bias $I_b(\omega - \Delta\omega)$ to the gauges, which are acting as signal mixers and measuring the potential at the bridge center. The output voltage at low frequency is proportional to

$$V_{out}(\Delta\omega) = \frac{1}{2} I_b \cdot \Delta R \cdot \cos(\Delta\omega t) \tag{3.79}$$

The two gauges situated on opposite sides of the lever work in tensile and compressive strain alternatively offering a double advantage. Firstly they allow making a differential measurement at the centre, working both at the same time, thus contributing twice on the output signal. Second this flexible design constitutes a balanced bridge configuration which permits suppression of the background at the middle point by applying two 180 degrees out of phase voltage signal to the gauges extremities. The adequate decoupling of actuation and detection by using orthogonal principles as well as separating them in frequency has a direct consequence on the background reduction. As shown in Fig. 3.15, a huge signal of the order of 2–3 mV at resonance and a very low background was obtained with these devices giving rise to a signal to background ratio of more than 60 dB.

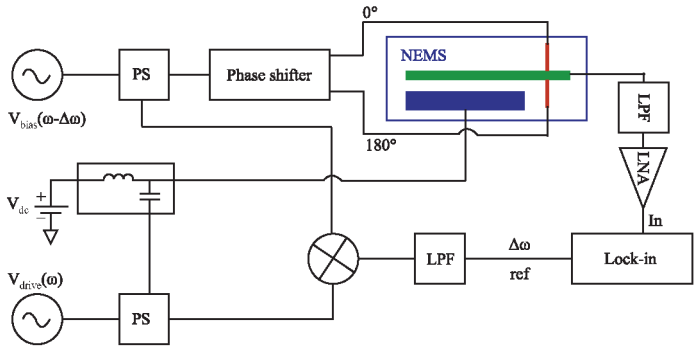

Figure 3.14 Test-bench for motion detection of piezoresistive resonant NEMS based on an ω down-mixing technique. PS, LPF are power splitter and phase shifter, respectively.

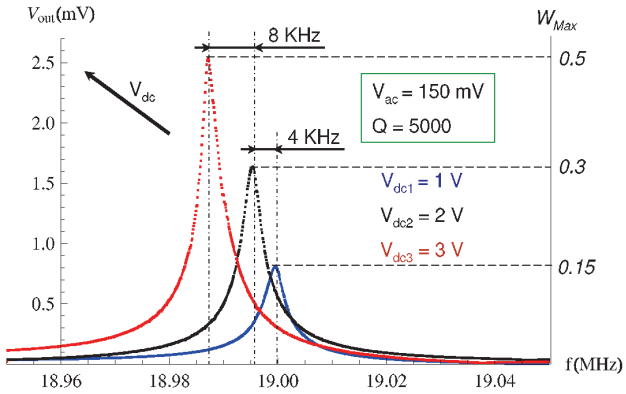

Figure 3.15 Linear resonance frequency responses measured using an ω zown-mixing technique. The effect of the DC voltage on the resonance frequency is presented.

Several measurements were performed on the device for a fixed bias voltage (V_{bias} = 1.56 V peak-peak). The cantilever displacement depends on the applied electrostatic force which is proportional to $F = \frac{1}{2}C\,(V_{\text{dc}} + V_{\text{ac}}\cos(\omega t))^2$. This force will have an AC ($F_{\text{ac}}(\omega)$) and a static (F_{dc}) component proportional to V_{dc}^2 for $V_{\text{dc}} >> V_{\text{ac}}$. The first will have a direct consequence on the displacement amplitude while the second affects the lever stiffness thus changing the resonance frequency. This is confirmed

by the experimental results showing that the resonance frequency curve shifts to the low frequencies due to the electrostatic negative stiffness (Fig. 3.15).

Figure 3.15 shows three linear resonance peaks obtained for V_{ac} = 150 mV and DC voltages going from 1 V up to 3 V. The analytical resonance frequency is around 21 MHz, while the measured one is around 19 MHz. This can be due to many factors such as silicon residual stress, size effect on Young's modulus as well as micro and nanofabrication tolerances. The measured quality factor of the first linear curve (V_{dc} = 1 V) is around 5000. Remarkably, increasing the DC voltage did not degrade the quality factor. In fact, in these devices, since the detection is piezoresistive, there is no correlation between the electrical resistance of the device and the measured quality factor. The expected dissipation from this mechanism (ohmic losses) is thus negligible. The last resonance curve of Fig. 3.15 (in red) is close to the critical amplitude that has been analytically computed using the developed model (Eq. (3.77) for a softening behavior), which results in $A_c \approx 90$ nm.

Then, in order to reach the nonlinear regime, the cantilever has been actuated using high DC voltages. Moreover, the frequency response has been tracked experimentally using a lock-in amplifier in frequency sweep-up and -down in order to obtain a full characterization of the resonator bifurcation topology. No extramechanism loss has been observed due to the nonlinear dynamics of the cantilever and therefore the same quality factor has been conserved (Q = 5000). Figure 3.16 shows two nonlinear resonance peaks:

- The first resonance curve (in dashed line) was obtained for V_{ac} = 150 mV and V_{dc} = 5 V. It displays a softening behavior characterized by a jump-up frequency at the bifurcation point B_2 and a jump-down frequency at the bifurcation point B_3 for which the cantilever oscillation amplitude is around 75% of the gap (150 nm).
- The second resonance curve was obtained for V_{ac} = 75 mV and V_{dc} = 8 V. Remarkably, in frequency sweep down, two jumps have been observed: a jump-up at the bifurcation point B_1 and a jump down at the highest bifurcation point in the softening domain B_3 for which the cantilever oscillation amplitude is around 150 nm. This characterizes a particular

mixed hardening-softening behavior (Kacem and Hentz, 2009), which is not the logical expected result since the increase in the DC voltage, amplifies the nonlinear negative stiffness due to the electrostatic forces. Combined with an oscillation amplitude below the first softening curve, this should ensure negligible mechanical nonlinearities with respect to the electrostatic nonlinearities. Hence, the dynamic behavior should be purely softening.

Nevertheless, in frequency sweep up, only a jump-up has been identified at the bifurcation point B_2. Then, the resonance response follows a softening branch. In this configuration, the nonlinear dynamic behavior of the cantilever is complex (between a softening and a mixed behavior) which leads to a sensitivity to the initial conditions.

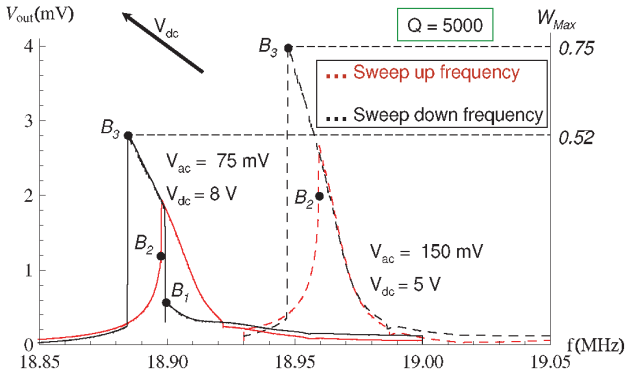

Figure 3.16 Nonlinear resonance frequency responses measured using an ω down-mixing technique and showing the location of the different bifurcation points $\{B_1, B_2$ and $B_3\}$. $W_{\max}$ is the cantilever displacement at its free end normalized by the gap.

3.4.7.2 Optimal DC voltage

For this piezoresistive resonant NEMS, the quality factor Q is constant with respect to the DC and AC voltages. Then, using Eqs. (3.76) and (3.77), the optimal DC drive voltage is

$$V_{dc_{OP}} = \sqrt{\frac{h^3 g^7}{2}\sqrt{\frac{1.65\times10^{39}}{(l-d)^{16}} + \frac{3.2\times10^{42}}{g^4(l-d)^{12}} - \frac{8.1\times10^{19}}{(l-d)^8}}} \tag{3.80}$$

The computed DC voltage that permits the hysteresis suppression is then computed using Eq. (3.80) resulting in $V_{dc_{OP}}$ = 1 V. Hence, a high AC voltage is needed in order to validate the nonlinearity cancellation. In practice and as shown in Fig. 3.15, the AC voltage should be higher than 0.5 V which makes the assumption of neglected second harmonic terms invalid and the used model must be corrected by including additional linear and nonlinear terms.

Nevertheless, one can use a 2ω configuration which enables the third order nonlinearity cancellation under primary resonance combined with a dynamic stabilization due to the superharmonic resonance (Kacem et al., 2011a).

3.4.7.3 2ω Down-mixing technique

In order to actuate the cantilever at its primary and super harmonic resonances simultaneously, a 2ω down-mixing technique has been used enabling a read-out of the resistance variation at a lower frequency $\Delta\omega$ (a schematic of the setup is shown in Fig. 3.17).

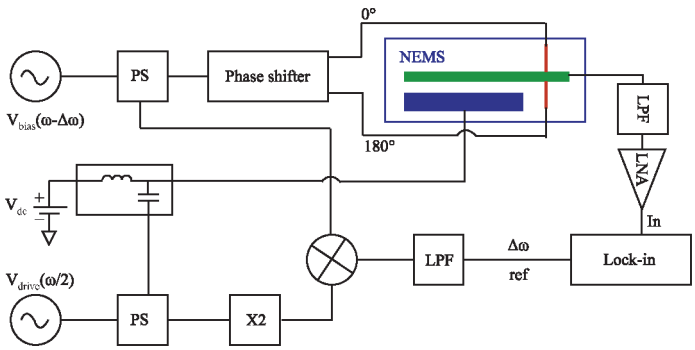

Figure 3.17 Test-bench for motion detection of piezoresistive resonant NEMS based on a 2ω down-mixing technique. PS, LPF are power splitter and phase shifter, respectively.

Several measurements were performed on the device for a fixed bias voltage (V_{bias} = 1.56 V peak-peak). The cantilever displacement depends on the applied electrostatic force which is proportional to $F = \frac{1}{2}C\left(V_{dc} + V_{ac}\cos\left(\frac{\omega}{2}t\right)\right)^2$. This force will have an AC ($F_{ac}(\omega)$) and a static (F_{dc}) component proportional to $V_{dc}^2 + \frac{1}{2}V_{ac}^2$.

Figure 3.18 shows two linear peaks obtained using a 2ω down-mixing technique for V_{ac} = 2 V. The measured quality factor is about 5000, which confirms the independence of Q on the DC and AC voltages. When, the DC voltage is increased from 0.2 V up to 0.3 V, the variation of the negative stiffness is negligible and consequently, no remarkable frequency shift has been observed. Interestingly, the measured output signal of the second linear peak is close to 3 mV for a low DC voltage, which was not reachable linearly for the ω down-mixing configuration.

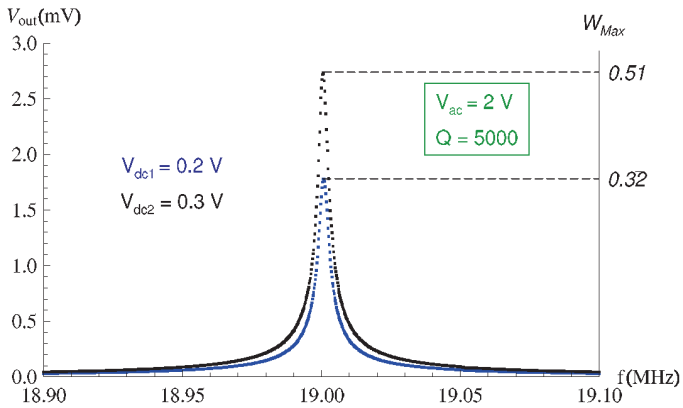

Figure 3.18 Linear resonance frequency responses measured using a 2ω down-mixing technique. The effect of the DC voltage on the resonance frequency is negligible. W_{max} is the cantilever displacement at its free end normalized by the gap.

Since the superharmonic resonance has no effect on the bistability limit of the resonator (Kacem et al., 2012), the mechanical critical amplitude of a cantilever under simultaneous resonance is then $A_{cm} = 6.3\frac{l}{\sqrt{Q}}$. However, in the electrostatic critical amplitude, one must add the contribution of the AC voltage in the nonlinear electrostatic stiffness, which changes substantially the close form solution of the optimal drive DC voltage. The latter has been estimated using the model for V_{ac} = 2 V resulting in V_{dc} = 0.5 V.

The resonance peak of Fig. 3.19 displays a slightly softening behavior close to the critical amplitude. The measured peak has been obtained using a 2ω down-mixing configuration for V_{ac} = 2 V

and V_{dc} = 0.5 V. Analytically, for this set of parameters the nonlinear electrostatic and mechanical stiffness's are balanced and the oscillation amplitude of the cantilever is close to 200 nm at its free end. Indeed, the maximum of induced stress into the piezoresistive gauges is reached, as the free end of cantilever touched the electrode without a damageable pull-in for which the cantilever becomes unstable and collapses. In order to verify that the pull-in amplitude has been reached, the DC voltage has been increased successively from 0.5 V up to 2 V. Consequently, the cantilever nonlinearity becomes potentially softening which should increase the oscillation amplitude of the NEMS sensor.

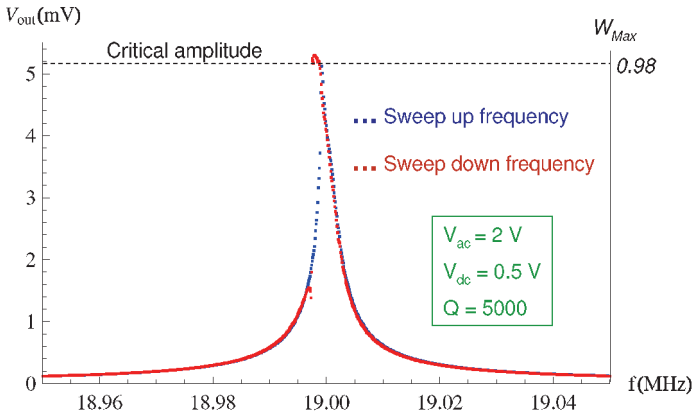

Figure 3.19 Slightly softening resonance frequency response measured using a 2ω down-mixing technique at the optimal DC voltage. The peak is close to the critical amplitude. Wmax is the cantilever displacement at its free end normalized by the gap.

Figure 3.20 shows a softening resonance curve obtained for V_{dc} = 2 V. The increase of the electrostatic softening nonlinear stiffness is displayed clearly by the distance between the two bifurcation points (softening domain) significantly enlarged in comparison with the frequency response in Fig. 3.18. Remarkably, the output signal at the peak is around 5.4 V which is the same value of V_{out} at V_{dc} = 0.5 V. Moreover, the slope of the softening branch between the two bifurcation points is close to zero, which confirms that the pull-in amplitude is reached giving the maximum of stress variation into the piezoresistive gauges.

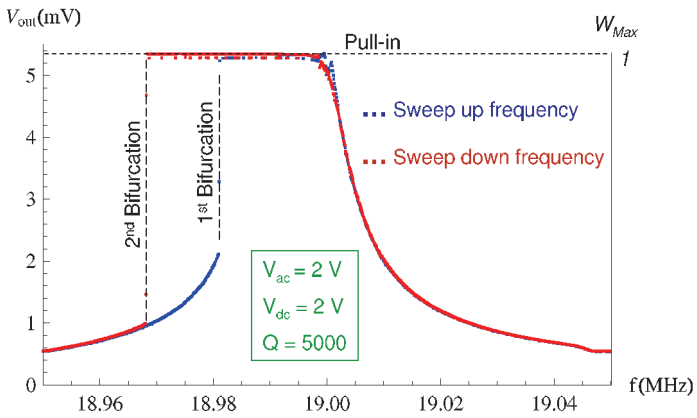

Figure 3.20 Softening frequency response measured using a 2ω down-mixing technique at V_{dc} = 2 V. The maximal stress on the piezoresistive gauges is reached for the pull-in amplitude. W_{max} is the cantilever displacement at its free end normalized by the gap.

3.4.8 Mass Resolution Enhancement

NEMS are usually embedded in a phase locked loop (PLL) or a self-excited loop in order to monitor time evolution of their resonant frequency. The frequency stability of the overall system (e.g., of the NEMS and the supporting electronics) is characterized by the Allan deviation, defined as (Mo Li and Roukes, 2007)

$$\frac{\delta\omega_0}{\omega_0} = \sqrt{\frac{1}{N-1}\sum_{1}^{N}\left(\frac{\overline{\omega}_{i+1}-\overline{\omega}_i}{\omega_0}\right)^2} \tag{3.81}$$

where ω_i is the average angular frequency in the i^{th} time interval, N is the number of independent frequency measurements, which is assumed to be a sufficiently large number. The mass resolution δm is then $\sqrt{2}M_{eff}\frac{\delta\omega_0}{\omega_0}$ for 1 second integration time. At the linear regime and for a cantilever oscillation amplitude around 65 nm, the dynamic range (DR) experimentally measured was about 100 dB (Mile et al., 2010). This would lead to a theoretical ultimate Allan deviation $\left.\frac{\delta\omega_0}{\omega_0}\right|_{th} = \frac{10^{-\frac{DR}{20}}}{\sqrt{2}Q}$ of around 10^{-9} (Ekinci et al., 2004). For an effective mass of 200 fg and a Q-

factor of 6500, this would result in a potential mass resolution of $\delta m = \frac{M_{\text{eff}}}{Q} 10^{-\frac{\text{DR}}{20}} \approx 0.3\,\text{zg}$ at room temperature and at relatively low frequency (20 MHz).

Using the drive conditions of Fig. 3.19, at an extremely enhanced critical amplitude of the gap order, the mass sensor dynamic range can be potentially enhanced to reach the level of 110 dB. Consequently, a resolution around 100 Da (0.1 zg) is achievable. However, to reach this performance, the temperature fluctuation should be controlled at least below 10^{-2} K (Giessibl, 2003). Actually, the experimental Allan deviation leads to a mass resolution of approximately 105 zg at room temperature (Mile et al., 2010).

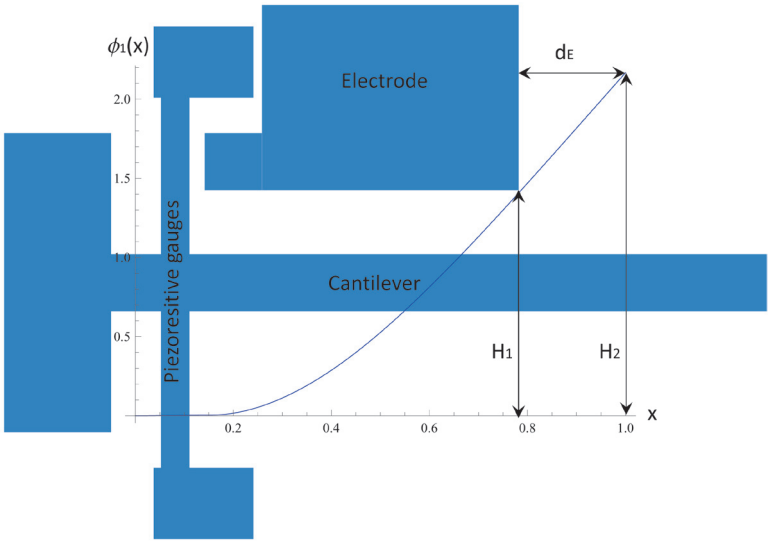

Figure 3.21 The next generation of NEMS resonant mass/gas sensor currently in fabrication in the clean rooms of LETI.

Once the noise contributions from the actuation voltage and the thermal bath issue are solved at low temperature, the ultimate resolution is then 100 Da. At this level, the cantilever probably touches the electrode as explained in Fig. 3.20. Consequently, no further optimizations are possible and one should think about a next generation of the studied device where the gap is quite larger than 200 nm. Nevertheless, the more we enlarge the gap,

the more the applied drive voltage must be significantly increased to achieve very high oscillations. Practically, one of the best solutions for the next generation of the NEMS resonant mass sensor consists in moving the actuation electrode closer to the piezoresistive gauges so that the free end of the cantilever is allowed to oscillate at amplitudes larger than the gap g. As shown in Fig. 3.21, the cantilever can potentially undergo oscillations of the order $\frac{H_2}{H_1}g$ at its free end. Combined with the use of an advanced top-down nanowire fabrication techniques (Ernst et al., 2008) with expected giant gauge factors, as well as a possible nonlinearity cancellation, this may greatly decrease the resolution down to one single Dalton.

3.5 Conclusions

In this chapter, the development of an analytical model and its validation to quantitatively assess the nonlinear dynamics of nanocantilever have been presented. This model includes the main sources of nonlinearities (mechanical and electrostatic) and is based on the modal decomposition using the Galerkin procedure combined with a perturbation technique (the averaging method).

As a first step, the experimental validation of the model has been performed on NEMS cantilevers fabricated using wafer-scale nanostencil lithography (nSL) enabling the definition of very low critical dimension devices. These cantilevers were monolithically integrated with CMOS circuits, which made possible the electrical characterization of their frequency responses. The NEMS devices have been driven in different conditions (in air and in vacuum). All parameters of the model, except the quality factor and the parasitic capacitance, are set prior to the comparison, which shows an excellent agreement in resonance frequency, peak shape and amplitude. Hence, it proves the efficiency of the model as a predictive tool.

The effects of some design parameters on the nonlinear behavior of nanocantilevers have been analytically investigated and close-form solutions of the critical amplitude under dominating mechanical nonlinearities and electrostatic nonlinearities, respectively, have been provided which demonstrates the large dynamic range of NEMS cantilevers compared to doubly clamped

nanobeams. The mechanical critical amplitude of a cantilever is then $A_{\mathrm{cm}} = 6.3\frac{l}{\sqrt{Q}}$ (Kacem et al., 2010). More specifically, the analytical expression of the optimal DC drive voltage has been extracted which is an interesting tool for resonant sensors designers. Theoretically, it allows for the cancellation of the nonlinearities in order to drive the NEMS cantilever linearly beyond its critical amplitude. Consequently, this may be a great gain in sensors' sensitivity, as the resonator's carrier power is largely increased while keeping a linear behavior; this may prevent most of noise mixing (Kaajakari et al., 2005a).

In a second step the model has been validated on a high frequency NEMS device electrostatically actuated based on piezoresistive detection (160 nm thick) fabricated using a hybrid e-beam/DUV lithography technique. The nanomechanical sensor has been characterized using a down-mixing technique. The ω configuration is first used in order to easily reach the nonlinear regime. Then, the optimal DC voltage being very low, a 2ω down-mixing configuration has been used in order to enable the compensation of the nonlinearities as predicted using the model.

The experimental results show an excellent agreement with the predicted dynamic behaviors. Particularly, the compensation of the nonlinearities has been validated for cantilever displacements up to the gap. Consequently and in a stable linear fashion, the optimal stress variation into the piezoresistive gauges has been reached using the 2ω down-mixing technique. Moreover, in this configuration the mixed behavior has not been observed up to the pull-in amplitude due to the effect of the superharmonic resonance in retarding and suppressing undesirable behaviors. An impressive ultimate resolution about 100 Da is achievable at low temperature and linearly at an oscillation amplitude comparable to the gap for which the maximum of strain collected by the piezoresistive gauges is reached. In order to overcome the gap limitation for the cantilever oscillations, the next generation of the studied device involves an actuation electrode shifted to the gauges side.

Very Large Scale Integration (VLSI) of such devices (Fig. 3.21) will potentially enable a wide range of new sensors, such as massive arrays of oscillating NEMS and sensitive multigas sensors. Indeed, the analytical rules provided in this chapter are applicable for resonant chemical and biological nanosensors in order to

ensure the optimal mass resolution. Hence, these nonlinear analyses could be very interesting for many nanotechnology challenges such as sub-single-atom resolution in NEMS mass spectrometry (Boisen, 2009).

Acknowledgments

I gratefully acknowledge financial support from the CARNOT institute (Carnot NEMS Project), from the ANR (MNTEurop Project) and from the European Commission within the project NaPa (contract no NMP4-CT-2003-500120). I am also pleased to acknowledge LETI and CNM clean room staff, LETI NEMS teams and Prof. Jürgen Brugger and his team (LMIS1) at EPFL for their contribution to sample processing.

References

Ahmadian, M., Borhan, H., and Esmailzadeh, E. (2009). Dynamic analysis of geometrically nonlinear and electrostatically actuated micro-beams. *Commun. Nonlinear Sci. Numerical Simulation*, **14**(4), 1627–1645.

Arafat, H. N., Nayfeh, A. H., and Chin, C.-M. (1998). Nonlinear nonplanar dynamics of parametrically excited cantilever beams. *Nonlinear Dynamics,* **15**, 31–61.

Arcamone, J., Misischi, B., Serra-Graells, F., van den Boogaart, M. A. F., Brugger, J., Torres, F., Abadal, G., Barniol, N., and Perez-Murano, F. (2007). A compact and low-power CMOS circuit for fully integrated NEMS resonators. *IEEE Trans. Circ. Syst. II: Expr. Briefs,* **54**(5), 377–381.

Arcamone, J., van den Boogaart, M. A. F., Serra-Graells, F., Fraxedas, J., Brugger, J., and Prez-Murano, F. (2008). Full-wafer fabrication by nanostencil lithography of micro/nanomechanical mass sensors monolithically integrated with CMOS. *Nanotechnology*, **19**(30), 305302.

Arlett, J. L., Maloney, J. R. B., Gudlewski, M. M., and Roukes, M. L. (2006). Self-sensing micro-and nanocantilevers with attonewton-scale force resolution. *Nano Lett.*, **6**(5), 1000–1006.

Bargatin, I., Myers, E. B., Arlett, J., Gudlewski, B., and Roukes, M. L. (2005). Sensitive detection of nanomechanical motion using piezoresistive signal downmixing. *App. Phys. Lett.*, **86**(13), 133109.

Boisen, A. (2009). Nanoelectromechanical systems: Mass spec goes nano-mechanical. *Nat. Nanotechnol.*, **4**, 404–405.

Bose, S., and Agarwal, G. S. (2006). Entangling pairs of nano-cantilevers, cooper-pair boxes and mesoscopic teleportation. *N. J. Phys.,* **8**(3), 34.

Chowdhury, S., Ahmadi, M., and Miller, W. C. (2005). A closed-form model for the pull-in voltage of electrostatically actuated cantilever beams. *J. Micromechan. Microeng.,* **15**(4), 756.

Cleland, A. N., and Roukes, M. L. (2002). Noise processes in nanomechanical resonators. *J. App. Phys.*, **92**(5), 2758–2769.

Colinet, E., Durand, C., Duraffourg, L., Audebert, P., Dumas, G., Casset, F., Ollier, E., Ancey, P., Carpentier, J.-F., Buchaillot, L., and Ionescu, A. (2009). Ultra-sensitive capacitive detection based on SGMOSFET compatible with front-end CMOS process. *IEEE J. Solid-State Circ.,* **44**(1), 247–257.

da Silva, M. R. M. C., and Zaretzky, C. L. (1994). Nonlinear flexural-flexural-torsional interactions in beams including the effect of torsional dynamics. (i) Primary resonance. *Nonlinear Dyn.*, **5**, 3–23.

Ekinci, K. L., and Roukes, M. L. (2005). Nanoelectromechanical systems. *Rev. Sci. Inst*., **76**(6), 061101.

Ekinci, K. L., Yang, Y. T., and Roukes, M. L. (2004). Ultimate limits to inertial mass sensing based upon nanoelectromechanical systems. *J. App. Phys.,* **95**(5), 2682–2689.

Ernst, T., Duraffourg, L., Dupré, C., Bernard, E., Andreucci, P., Becu, S., Ollier, E., Hubert, A., Halte, C., Buckley, J., Thomas, O., Delapierre, G., Deleonibus, S., De Salvo, B., Robert, P., and Faynot, O. (2008). Novel Si-based nanowire devices: Will they serve ultimate MOSFETs scaling or ultimate hybrid integration? in Electron Devices Meeting, 2008. IEDM 2008. IEEE International, pp. 1–4.

Geller, M. R., and Varley, J. B. (2005). Friction in nanoelectromechanical systems: Clamping loss in the GHz regime, http://arxiv.org/abs/cond-mat/0512710v1.

Giessibl, F. J. (2003). Advances in atomic force microscopy. *Rev. Mod. Phys*., **75**(3), 949–983.

Hao, Z., Erbil, A., and Ayazi, F. (2003). An analytical model for support loss in micromachined beam resonators with in-plane flexural vibrations. *Sens. Actuators A Phys.,* **109**(1–2), 156–164.

He, R., Feng, X. L., Roukes, M. L., and Yang, P. (2008). Self-transducing silicon nanowire electromechanical systems at room temperature. *Nano Lett.,* **8**(6), 1756–1761.

He, R., and Yang, P. (2006). Giant piezoresistance effect in silicon nanowires. *Nat. Nanotechnol.,* **1**, 42–46.

Jensen, K. Girit, C., Mickelson, W., and Zettl, A. (2006). Tunable nanoresonators constructed from telescoping nanotubes. *Phys. Rev. Lett.*, **96**(21), 215503.

Jiang, Y. G., Ono, T., and Esashi, M. (2008). Fabrication of piezoresistive nanocantilevers for ultra-sensitive force detection. *Meas. Sci. Technol.*, **19**(8), 084011.

Juillard, J., Bonnoit, A., Avignon, E., Hentz, S., Kacem, N., and Colinet, E. (2008). From MEMS to NEMS: Closed-loop actuation of resonant beams beyond the critical Duffing amplitude. *in Sensors, 2008 IEEE*, pp. 510–513.

Kaajakari, V., Koskinen, J., and Mattila, T. (2005a). Phase noise in capacitively coupled micromechanical oscillators, *IEEE Trans. Ultrason. Ferroelectr. Freq. Control.,* **52**(12), 2322–2331.

Kaajakari, V., Koskinen, J. K., and Mattila, T. (2005b). Phase noise in capacitively coupled micromechanical oscillators. *IEEE Trans. Ultrason. Ferroelectr. Freq. Control.,* **52**(12), 2322–2331.

Kacem, N., Arcamone, J., Perez-Murano, F., and Hentz, S. (2010). Dynamic range enhancement of nonlinear nanomechanical resonant cantilevers for highly sensitive NEMS gas/mass sensor applications. *J. Micromechan. Microeng.*, **20**(4), 045023.

Kacem, N., Baguet, S., Dufour, R., and Hentz, S. (2011a). Stability control of nonlinear micromechanical resonators under simultaneous primary and superharmonic resonances. *App. Phys. Lett.*, **98**(19), 193507.

Kacem, N., Baguet, S., Hentz, S., and Dufour, R. (2011b). Computational and quasi-analytical models for nonlinear vibrations of resonant MEMS and NEMS sensors, *Int. J. Nonlinear Mechan.,* **46**(3), 532–542.

Kacem, N., and Hentz, S. (2009). Bifurcation topology tuning of a mixed behavior in nonlinear micromechanical resonators. *App. Phys. Lett.*, **95**(18), 183104.

Kacem, N., Hentz, S., Hentz, S., and Dufour, R. (2012). Pull-in retarding in nonlinear nanoelectromechanical resonators under super-harmonic excitation. *J. Computat. Nonlinear Dyn.*, **7**(2), 021011.

Kacem, N., Hentz, S., Pinto, D., Reig, B., and Nguyen, V. (2009). Nonlinear dynamics of nanomechanical beam resonators: Improving the performance of NEMS-based sensors. *Nanotechnology*, **20**(27), 275501.

Li, M., Tang, H. X., and Roukes, M. L. (2007). Ultra-sensitive NEMS-based cantilevers for sensing, scanned probe and very high-frequency applications. *Nat. Nanotechnol.*, **2**, 114–120.

Lifshitz, R., and Roukes, M. L. (2000). Thermoelastic damping in micro-and nanomechanical systems. *Phys. Rev. B*, **61**(8), 5600–5609.

Liu, S., Davidson, A., and Lin, Q. (2004). Simulation studies on nonlinear dynamics and chaos in a MEMS cantilever control system. *J. Micromechan. Microeng.*, **14**(7), 1064.

Mile, E., Jourdan, G., Bargatin, I., Labarthe, S., Marcoux, C., Andreucci, P., Hentz, S., Kharrat, C., Colinet, E., and Duraffourg, L. (2010). In-plane nanoelectromechanical resonators based on silicon nanowire piezoresistive detection. *Nanotechnology*, **21**(16), 165504.

Mo, Li, H. X. T., and Roukes, M. L. (2007). Ultra-sensitive NEMS-based cantilevers for sensing, scanned probe and very high-frequency applications. *Nat. Nanotechnol.*, **2**, 114–120.

Mohanty, P., Harrington, D. A., Ekinci, K. L., Yang, Y. T., Murphy, M. J., and Roukes, M. L. (2002). Intrinsic dissipation in high-frequency micromechanical resonators. *Phys. Rev. B*, **66**(8), 085416.

Nayfeh, A. H., and Pai, P. F. (1989). Nonlinear non-planar parametric responses of an inextensional beam. *Int. J. Nonlinear Mechan.*, **24**, 139–158.

Nayfeh, A. H., Younis, M. I., and Abdel-Rahman, E. M. (2007). Dynamic pull-in phenomenon in MEMS resonators. *Nonlinear Dyn.*, **48**, 153–163.

Nishiyama, H., and Nakamura, M. (1990). Capacitance of a strip capacitor. *IEEE Trans. Components Hybrids Manufacturing Technol.*, **13**(2), 417–423.

Pai, P. F., and Nayfeh, A. H. (1990). Nonlinear nonplanar oscillations of a cantilever beam under lateral base excitations. *Int. J. Nonlinear Mechan.*, **25**, 455–474.

Postma, H. W. C., Kozinsky, I., Husain, A., and Roukes, M. L. (2005). Dynamic range of nanotube-and nanowire-based electromechanical systems, *Appl. Phys. Lett.*, **86**(22), 223105.

Robins, W. P. (1982). Phase noise in signal sources: Theory and applications, IEE Telecommunications Series, Publish by Peregrinus, ISBN 978-090-6048-76-4, LCCN 82208863.

Roessig, T. (1998). Integrated MEMS tuning fork oscillators for sensor applications, Ph.D. thesis, University of California, Berkeley.

Roessig, T. A., Howe, R. T., and Pisano, A. P. (1997). Nonlinear mixing in surface-micromachined tuning fork oscillators. in *Frequency Control Symposium 1997*. *Proceedings of the 1997 IEEE International.*, pp. 778–782.

Sazonova, V. A. (2006). A tunable carbon nanotube resonator, Ph.D. thesis, Cornell University.

Silva, M. R. M. C. D. (1988a). Nonlinear flexural-flexural-torsional-extensional dynamics of beams. i: Formulation. *Int. J. Solids Struct.,* **24**, 1225–1234.

Silva, M. R. M. C. D. (1988b). Nonlinear flexural-flexural-torsional extensional dynamics of beams. ii: Response analysis. *Int. J. Solids Struct.,* **24**, 1235–1242.

Silva, M. R. M. C. D., and Glynn, C. C. (1978a). Nonlinear flexural-flexural-torsional dynamics of inextensional beams. i: Equations of motion. *J. Struct. Mechan.,* **6**, 437–448.

Silva, M. R. M. C. D., and Glynn, C. C. (1978b). Nonlinear flexural-flexural-torsional dynamics of inextensional beams. i: Equations of motion. *J. Struct. Mechan.,* **6**, 437–448.

Silva, M. R. M. C. D., and Glynn, C. C. (1978c). Nonlinear flexural-flexural-torsional dynamics of inextensional beams. ii: Forced motions. *J. Struct. Mechan.,* **6**, 449–461.

Silva, M. R. M. C. D., and Glynn, C. C. (1978d). Nonlinear flexural-flexural-torsional dynamics of inextensional beams. ii: Forced motions. *J. Struct. Mechan.,* **6**, 449–461.

Van den Boogaart, M., Kim, G., Pellens, R., Van den Heuvel, J. P., Brugger, J. (2004). Deep-ultraviolet microelectromechanical systems stencils for high-throughput resistless patterning of mesoscopic structures. *J. Vac. Sci. Technol*., B, **22**, 3174–3178.

Verd, J., Uranga, A., Abadal, G., Teva, J., Torres, F., Lopez, J., Perez-Murano, E., Esteve, J., and Barniol, N. (2008). Monolithic CMOS MEMS oscillator circuit for sensing in the attogram range. *Electron Device Lett. IEEE,* **29**(2), 146–148.

Verd, J., Uranga, A., Teva, J., Lopez, J., Torres, F., Esteve, J., Abadal, G., Perez-Murano, F., and Barniol, N. (2006). Integrated CMOS MEMS with on-chip readout electronics for high-frequency applications. *IEEE Electron Device Lett*., **27**(6), 495–497.

Yang, Y. T., Callegari, C., Feng, X. L., Ekinci, K. L., Roukes, M. L. (2006). Zeptogram-scale nanomechanical mass sensing. *Nano Lett.,* **6**(4), 583–586.

Yang, J., Ono, T., and Esashi, M. (2002). Energy dissipation in submicrometer thick single-crystal silicon cantilevers. *J. Microelectromechan. Syst*., **11**(6), 775–783.

Yurke, B., Greywall, D. S., Pargellis, A. N., and Busch, P. A. (1995). Theory of amplifier-noise evasion in an oscillator employing a nonlinear resonator. *Phys. Rev. A*, **51**(5), 4211–4229.

Zaretzky, C. L., and da Silva, M. R. M. C. (1994). Nonlinear flexural-flexural-torsional interactions in beams including the effect of torsional dynamics. ii: Combination resonance. *Nonlinear Dyn.*, **5**, 161–180.

Zener, C. (1938). Internal friction in solids ii. general theory of thermoelastic internal friction. *Phys. Rev.*, **53**(1), 90–99.